Multi-Modal Unsupervised Change Detection of Urban Vegetation in Birmingham, UK: A Cross-Method Comparison under 2022 Drought Conditions

Naya Desai*[1], Emma J.S. Ferranti†[1], Sarah V. Greenham‡[1], Joshua Vande Hey§[2], Andrew D. Quinn¶[1], and Stef De Sabbata‖[3]

[1]School of Engineering, University of Birmingham, Birmingham, B15 2FG, UK
[2]School of Physics and Astronomy, University of Leicester, Leicester, LE1 7RH, UK
[3]School of Geography and Geology, University of Leicester, Leicester, LE1 7RH, UK

This manuscript is a non-peer-reviewed preprint submitted to *EarthArXiv*.

*Corresponding author: nxd379@student.bham.ac.uk
†e.ferranti@bham.ac.uk
‡s.greenham@bham.ac.uk
§jvh7@le.ac.uk
¶a.d.quinn@bham.ac.uk
‖s.desabbata@leicester.ac.uk

Abstract

As the climate changes, cities are increasingly exposed to extreme weather events such as droughts, further amplified by the *urban heat island effect*. Urban vegetation, a key Nature-based Solution for cooling and climate resilience, is vulnerable to water stress. Therefore, it is increasingly important to understand how urban vegetation responds during drought years, particularly where ground-truth data are limited. This study investigates vegetation change across Birmingham, UK, using three unsupervised change detection techniques that require neither labeled nor ground-truth data. A multi-modal dataset was leveraged by combining optical (Sentinel-2) and C-band radar (Sentinel-1) observations through decision-level fusion. Three approaches were applied to the bitemporal composites from July 2021 (non-drought year) and July 2022 (drought year): (i) baseline image differencing with k-means clustering; (ii) floating references; and (iii) pre-trained representation learning via the Clay foundation autoencoder. Three methods demonstrated complementary strengths. Baseline differencing provided simplicity, speed, and reliable performance for fine-scale urban analysis at 10 m, although single-sensor detections were more susceptible to misclassifications of vegetation change due to rooftop-driven artefacts. The floating references method, operating at 10 m, reduced bias from inter-scene drift and illumination differences, proving particularly effective for detecting agricultural sensitivity; however, it required greater computational demand. Meanwhile, the Clay-derived binary change map, generated through principal component analysis and Otsu's thresholding, produced spatially coherent and semantically rich vegetation change patterns, though its coarser effective resolution ($\sim$80 m) likely smoothed fine-scale artefacts and contributed to higher spatial coherence, limiting direct comparison with the 10 m methods. Overall, the resulting change maps offer valuable and complementary insights for urban vegetation management under a changing climate, thereby supporting the use of unsupervised multi-sensor approaches for vegetation monitoring in data-scarce urban environments. Future work should explore the incorporation of L-band radar, the generation of a consensus agreement map for species-level change analysis, the examination of soft clustering algorithms, and an expansion of the regional scope to quantify drought-associated vegetation change across broader regions.

Keywords: change detection; unsupervised machine learning; multi-modal remote sensing; urban vegetation; geospatial analysis

1 Introduction

Global mean surface temperatures are rising under climate change [59], leading to intensified extreme weather events, such as droughts [59, 104]. Whilst the term for drought is not universally defined, it is broadly considered as an abnormal precipitation deficit, often accompanied by increased heat [96]. The UK experienced a prolonged drought in the summer of 2022, which was one of the hottest and fifth driest summers since the 1890s [91]. Subsequently, the drought had extensive impacts and generated discussions on the climate resilience of the UK in the context of anthropogenic warming [7].

Moreover, urbanized environments are particularly susceptible to the harmful effects of droughts due to the *urban heat island effect* [70], whereby cities experience increased temperatures relative to their rural surroundings. Urban greenery is a widely accepted Nature-based Solution (NbS) due to vegetation's ability to cool down its surroundings through evapotranspiration and shade, as shown by Ferranti et al. [35] and references therein.

However, in order to optimize the cooling ecosystem services of urban vegetation, it must be healthy and properly hydrated [30, 36, 80]. Drought can strongly affect vegetation growth by disrupting physiological and ecological processes, leading to ecosystem degradation [38, 103]. For example, for leafy vegetation such as trees, drought stress can prompt stomata closure, resulting in a decrease in transpiration and photosynthesis rates [17]. Reduction in photosynthesis activity coupled with water deprivation can increase heat dissipation, modify chlorophyll fluorescence, and reduce leaf water content [48]. Overall, drought stress can ultimately lead to leaf shedding and crown dieback. Therefore, city planners and policymakers must understand vegetation change associated with drought to establish necessary maintenance routines (e.g., watering in drought-sensitive areas) to better support vegetation health in order to maximize its cooling benefits.

Historically, assessments of vegetation health relied on in-situ observations. With the advancement of remote sensing, monitoring became possible at larger spatial scales, enabling systematic evaluation of vegetation condition across the Earth's surface using both optical and radar instruments. Optical data provide the means to quantify vegetation health through spectral vegetation indices (SVIs) such as the Normalized Difference Vegetation Index (NDVI), Normalized Difference Moisture Index (NDMI), and Soil Adjusted Vegetation Index (SAVI) [96]. Numerous studies have demonstrated the efficacy of Sentinel-2 and SVIs for drought assessment [31, 52, 53, 67, 93]. NDVI offers a robust measure of greenness, NDMI captures canopy moisture variability and provides early indicators of hydrological stress, and SAVI, similar to NDVI, quantifies greenness with the additional consideration of soil reflectance, which is crucially important in sparsely vegetated environments such as urban areas.

In addition, radar observations from Sentinel-1 have proven valuable for vegetation monitoring through their sensitivity to the dielectric and geometric properties of vegetation canopies. Variations in backscatter and polarization capture changes in vegetation structure and moisture content [95], allowing Sentinel-1 data to be applied effectively for drought monitoring [88, 92]. Each modality, however, has inherent limitations. Sentinel-2 is affected by cloud cover and atmospheric interference, whereas Sentinel-1 is susceptible to speckle noise, which can reduce image accuracy. Thus, relying on a single sensor can introduce bias or uncertainty in estimating

vegetation stress. To overcome these limitations, multi-modal data fusion has become a vital approach for producing more reliable and comprehensive representations of vegetation health [85].

One key application where multi-modal fusion has proven especially powerful is change detection, which compares bitemporal imagery to analyze and identify differences in the landscape caused by specific phenomena. Recent studies have demonstrated the effectiveness of multi-modal change detection for earthquake damage assessment [20], land cover change [57], urban change [8, 41], and agricultural drought monitoring [39]. Furthermore, with advances in artificial intelligence, unsupervised machine learning (ML) has gained prominence for change detection [69, 75, 84]. Unsupervised ML is particularly advantageous in data-scarce contexts, as it does not require labeled data, which is often a limiting factor in remote sensing and change detection studies [45]. Instead, it autonomously uncovers latent patterns within the data that may be unbeknownst to the human eye [68].

Early work by Zheng et al. [105] demonstrated the power of simple image differencing combined with k-means for change detection, while Moco et al. [66] showed that floating references offer state-of-the-art performance among more complex unsupervised techniques. More recently, deep learning, such as foundation models, has become increasingly central to change mapping [25, 50, 76, 85, 99]. However, a key challenge in unsupervised change detection lies in the absence of ground-truth data for accuracy assessment. Consequently, validation strategies often rely on independent spatial and thematic indicators. Recent studies highlight the utility of combining global land cover datasets with spatial autocorrelation metrics to assess the spatial coherence and thematic plausibility of detected change patterns [45, 71, 84, 87].

Nonetheless, fusing multi-modal datasets remains challenging due to inter-sensor misalignment and differences in data distribution, making it non-trivial to decide whether fusion should occur at the feature or decision level. However, Yousif et al. [101] found that decision-level fusion was especially effective when paired with unsupervised ML and change detection.

Despite progress in these areas, the integration of such approaches for urban vegetation change analysis remains limited, as previous urban drought studies have largely leveraged single sensors for change detection [43, 63, 79]. Further, whilst unsupervised change detection, multi-sensor fusion, and foundation model approaches have all been studied in remote sensing, relatively limited work has compared these approaches within a single city-scale framework for urban vegetation change associated with a drought year. This study therefore aims to address this gap by examining urban vegetation change associated with the 2022 drought in Birmingham, UK through an unsupervised ML approach in Python (v 3.11.3). Notably, the detected changes are interpreted as vegetation change associated with the 2022 drought summer, while acknowledging broader interannual variability may also be captured. The workflow leverages three different methods: (i) baseline image differencing with k-means; (ii) floating references; and (iii) Clay [90], a geospatial, foundation deep learning model. This study evaluates how each technique differs in spatial pattern, selectivity, conservativeness, and interpretability of vegetation change identified between a non-drought reference summer and the 2022 drought summer.

2 Materials and Methods

2.1 Study Area

The area of interest (AOI) for this study was Birmingham, UK (Figure 1). Birmingham is the UK's second largest city with about 1.1 million residents [13]. It is located within the West Midlands administrative boundary (lat. 52.4823°, long. 1.8900°), covering 268 km^2.

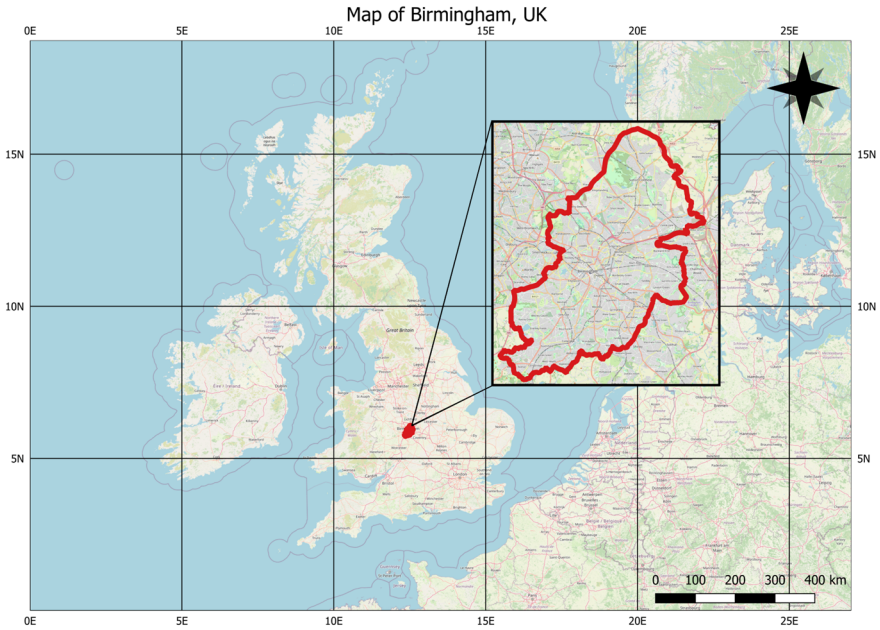

Figure 1: Boundary of Birmingham within the UK.

Birmingham currently comprises approximately 600 greenspaces and Birmingham City Council has plans to increase this to 1,000 in the next 25 years [10, 15]. The city has over one million trees and 1,398 hectares of woodlands, with its tree canopy spanning 48.81 km^2. Birmingham has achieved 'Tree City of the World' status for 6 consecutive years [11] while additionally being declared the UK's first accredited '*Nature City*' [12] - an initiative that recognizes the city's commitment to providing more and better urban greenery.

Table 1: Meteorological context for the July 2021 and July 2022 comparison period. The July climatology was calculated over 2011-2021, and the 2022 anomaly was computed relative to this baseline.

Variable	**July 2021**	**July 2022**	**July Climatology**	**2022 Anomaly**
Mean air temperature (°C)	18.20	18.51	17.19	+1.32
Total precipitation (mm)	142.40	47.60	113.20	-65.60

Moreover, to contextualize drought in Birmingham, local meteorological observations were summarized for July 2021 and July 2022 (Table 1). Meteorological observations were obtained from the MIDAS Open archive for a Birmingham station, including daily temperature data [61] and hourly rainfall data [62] from the Met Office via the Centre for Environmental Data Analysis (CEDA). Relative to the 2011-2021 July climatology, July 2022 was both warmer and

markedly drier, with mean air temperature 1.32 °C above the long-term July average and total precipitation 65.6 mm below it.

2.2 Data

This study is underpinned by optical and radar data from Sentinel-2 (S2) [34] and Sentinel-1 (S1) [33], both accessed via the Google Earth Engine (GEE) platform. The bitemporal imagery acquired for change detection at epoch t is denoted by $\mathbf{x}_t^{\mathrm{S1}}$ and $\mathbf{x}_t^{\mathrm{S2}}$, respectively. Let $\mathcal{D}$ represent the multi-modal dataset, which comprises the bitemporal image-pair instances

$$\mathcal{D} = (\mathbf{x}_{t_1}^{\mathrm{S1}}, \mathbf{x}_{t_2}^{\mathrm{S1}}, \mathbf{x}_{t_1}^{\mathrm{S2}}, \mathbf{x}_{t_2}^{\mathrm{S2}}),$$

where t_1 and t_2 represent the July 2021 and July 2022 monthly composites. July 2021 was selected as the baseline (pre-drought) year due to the absence of drought conditions across the UK and the availability of a cloud-free Sentinel-2 composite for that summer, ensuring an undisturbed vegetation state. This provided a stable reference against which the July 2022 drought impacts could be quantified.

2.2.1 Sentinel-2

Sentinel-2 is a constellation of sun-synchronous satellites equipped with multispectral imagers (MSI) providing a 10-day revisit time per satellite. Until 2024, the constellation comprised two twin satellites, Sentinel-2A and Sentinel-2B. For this study, Sentinel-2 Level-2A monthly median composites were obtained for the red (Band 4), blue (Band 2), green (Band 3), near-infrared (NIR, Band 8), and short-wave infrared (SWIR, Band 11) bands at 10 m and 20 m resolution.

As the imagery was already atmospherically and radiometrically corrected at Level-2A [31], preprocessing focused on spatial alignment and harmonization. Within GEE, the Birmingham boundary vector shapefile was handled in the EPSG:4326 coordinate reference system (CRS) for compatibility. The downloaded composites were therefore reprojected to EPSG:4326 to ensure spatial alignment during clipping, after which pixels outside the Birmingham boundary were masked. Following standard practice, the SWIR band was resampled to 10 m spatial resolution using bilinear interpolation [54]. This resampling step is crucial in maintaining high spatial detail in a heterogeneous urban environment and ensures that all bands are of the same spatial resolution. Finally, $x_{t_1}^{\mathrm{S2}}$ and $x_{t_2}^{\mathrm{S2}}$ were co-registered to correct for any aleatory or systematic geolocation offsets, which is crucial for accurate image-to-image comparison [18].

Subsequently, NDVI [81], NDMI [37], and SAVI [46] were calculated for each composite using Equations (1)-(3). For SAVI, a soil-brightness correction factor $L = 0.5$ [1] was applied to minimize the influence of exposed soil in sparsely vegetated areas.

$$NDVI = \frac{(NIR - Red)}{(NIR + Red)} \tag{1}$$

$$NDMI = \frac{(NIR - SWIR)}{(NIR + SWIR)} \tag{2}$$

$$SAVI = \frac{(NIR - Red)}{NIR + Red + L} * (1 + L) \tag{3}$$

2.2.2 Sentinel-1

Similarly, Sentinel-1 is a two-satellite constellation comprising Sentinel-1A and Sentinel-1B (until December 2021), operating in a sun-synchronous orbit with a 12-day repeat cycle per satellite. Sentinel-1 carries a C-band Synthetic Aperture Radar (SAR) instrument, thereby enabling continuous imaging of the Earth's surface through all weather, day and night.

Sentinel-1 Ground Range Detected (GRD) data were obtained from GEE, selecting only interferometric wide (IW) swath scenes acquired with dual polarization (VV, VH). GEE was particularly advantageous as it provides analysis-ready Sentinel-1 data that has already undergone standard preprocessing, including calibration, thermal noise removal, terrain correction, and $10\log_{10}$ scaling to decibel (dB). Although the imagery has an effective spatial resolution of approximately 20 m, it is provided on a 10 m pixel grid, thereby supporting alignment with Sentinel-2.

To acquire each $x_{t_1}^{\mathrm{S1}}$ and $x_{t_2}^{\mathrm{S1}}$ composite, both ascending and descending acquisitions were counted over the AOI and the orbit with the greater number of images was selected; consequently, the descending orbit was chosen for the entire analysis period. Following the workflow of [42], backscatter values below -25 dB were masked on a per-image, per-band basis, and the per-pixel temporal mean in dB was then computed for both VV and VH across all valid scenes within each month, yielding the `VV_mean_dB` and `VH_mean_dB` bands. The per-pixel mean incidence angle was retained as an auxiliary band, and native edge and noise masks from the GRD products were preserved throughout.

To mitigate the influence of extreme outliers, each Sentinel-1 composite was winsorized by capping VV and VH backscatter at the 99.9th percentile, computed once from the $x_{t_1}^{\mathrm{S1}}$ composite and applied consistently to $x_{t_2}^{\mathrm{S1}}$ to maintain interannual comparability and to avoid conditioning thresholds on the drought-affected distribution in 2022. All mosaics were then reprojected to EPSG:4326 using bilinear resampling, which is appropriate for continuous data [94]. The reprojected images were masked to exclude pixels outside the AOI boundary, and the $x_{t_1}^{\mathrm{S1}}$ and $x_{t_2}^{\mathrm{S1}}$ mosaics were validated for co-registration by confirming identical coordinate systems, geotransforms, raster dimensions, and pixel alignment. Together, these steps ensured that all Sentinel-1 inputs were radiometrically robust, spatially consistent, and directly comparable across both epochs.

2.3 Change Detection Methods

Three different methodologies were investigated for demarcating vegetation change associated with the 2022 drought. These methods were chosen due to their computational efficiency and ability to ascertain change without the need for labeled training data. Furthermore, each method presents differing advantages, which are discussed in more detail in Section 3.3.

The computational analysis designed in this research was conducted in Python (v 3.11.3) on a CPU-based high-performance computing (HPC) system. The workflow employed standard scientific and geospatial Python libraries such as NumPy, Rasterio, GeoPandas, and scikit-learn.

Where stochastic procedures were used, including clustering, fixed random states (`random_state = 42`) were applied to improve reproducibility.

2.3.1 Baseline Image Differencing

The first and baseline technique used to detect drought-related change was image differencing, a widely adopted pixel-based change detection approach [47]. In this framework, bitemporal composites from pre-change (t_1) and post-change (t_2) epochs were subtracted to quantify spectral or backscatter change at each pixel defined as:

$$\Delta \mathbf{x}^{\mathrm{S2}} = \mathbf{x}_{t_2}^{\mathrm{S2}} - \mathbf{x}_{t_1}^{\mathrm{S2}} \tag{4}$$

$$\Delta \mathbf{x}^{\mathrm{S1}} = \mathbf{x}_{t_2}^{\mathrm{S1}} - \mathbf{x}_{t_1}^{\mathrm{S1}} \tag{5}$$

For Sentinel-2 imagery, each $\mathbf{x}_{t_1}$ and $\mathbf{x}_{t_2}$ composite comprised stacked values of NDVI, NDMI, and SAVI, whilst the Sentinel-1 stack consisted of VV and VH backscatter values and their polarization ratio (VV-VH).

To enhance comparability across variables and reduce the influence of outliers, all features were standardized using z-score normalization [97], such that each variable had zero mean and unit variance across valid pixels, producing standardized change vectors $\Delta \mathbf{x}^{\mathrm{S2,std}}$ and $\Delta \mathbf{x}^{\mathrm{S1,std}}$. For optical data, standardized values were further clipped to the range $[-3, 3]$, retaining approximately 99.7% of observations under the assumption of normality [49], thereby minimizing the impact of extreme outliers on clustering. The radar features were already winsorized during preprocessing, so no additional clipping was required.

After feature standardization, k-means clustering with $K = 4$ was applied separately to $\Delta \mathbf{x}^{\mathrm{S2,std}}$ and $\Delta \mathbf{x}^{\mathrm{S1,std}}$ to partition pixels into groups representing different magnitudes of change. The choice of $K = 4$ was selected using the *elbow method* [102], which indicated that four clusters provided a suitable balance between capturing meaningful structure in the differenced feature space and avoiding unnecessary over-partitioning. Unlike binary thresholding, this enabled a more nuanced interpretation of vegetation change by highlighting varying degrees of change across the study area. Subsequently, only the cluster exhibiting the strongest negative change across variables was retained and interpreted as representing drought-affected areas because vegetation change associated with drought is expected to correspond to a decline in spectral greenness, moisture, or radar backscatter.

However, the k-means algorithm is applied only to the values themselves, without taking into account the 2D structure of the data. Thus, a key limitation of this method lies in the need to flatten the spatial data, which results in the loss of spatial structure and contextual information.

2.3.2 Floating References

To reduce bias from fixed baselines and improve robustness to inter-scene drift, the floating references (FR) change detection approach was adopted following [66, 69]. In this approach,

change is assessed relative to an adaptive, data-driven reference derived from the combination of both epochs (t_1 and t_2), rather than a fixed image.

All pixels across both epochs were jointly clustered via k-means with $K = 20$ for each remote sensing modality separately, producing centroids $\{\boldsymbol{\mu}_k\}_{k=1}^{K}$ that represent the underlying spectral and textural modes of the scene. $K = 20$ was utilized to provide a finer partitioning of the joint feature space. Contrasting the baseline differencing approach, which aimed to separate broad magnitudes of change, the FR framework required a larger number of clusters to represent heterogeneous urban surfaces, vegetation states, and mixed spectral responses [44] across the two epochs, therefore, acting as a pragmatic balance between sensitivity to scene heterogeneity and computational tractability.

Let $\mathbf{x}_i$ and $\mathbf{y}_i$ denote the feature vectors of pixel i in the t_1 and t_2 composites, respectively. Each pixel i was assigned to a cluster k_j and residuals were computed relative to its local floating reference as:

$$\delta_{x,i}^{\mathrm{S1}} = \mathbf{x}_i^{\mathrm{S1}} - \boldsymbol{\mu}_{k_j}^{\mathrm{S1}} \tag{6}$$

$$\delta_{y,i}^{\mathrm{S1}} = \mathbf{y}_i^{\mathrm{S1}} - \boldsymbol{\mu}_{k_j}^{\mathrm{S1}} \tag{7}$$

$$\delta_{x,i}^{\mathrm{S2}} = \mathbf{x}_i^{\mathrm{S2}} - \boldsymbol{\mu}_{k_j}^{\mathrm{S2}} \tag{8}$$

$$\delta_{y,i}^{\mathrm{S2}} = \mathbf{y}_i^{\mathrm{S2}} - \boldsymbol{\mu}_{k_j}^{\mathrm{S2}} \tag{9}$$

A per-pixel change magnitude was then estimated as the Euclidean distance between residuals:

$$D_i^{\mathrm{S1}} = \|\delta_{y,i}^{\mathrm{S1}} - \delta_{x,i}^{\mathrm{S1}}\| \tag{10}$$

$$D_i^{\mathrm{S2}} = \|\delta_{y,i}^{\mathrm{S2}} - \delta_{x,i}^{\mathrm{S2}}\| \tag{11}$$

Pixels with D_i values exceeding an empirical threshold (97.5th percentile of D_i) were classified as "changed." The 97.5th percentile was adopted through isolating the upper tail of the dissimilarity distribution, thereby identifying the most pronounced departures from the floating reference.

As this study specifically targeted negative vegetation or moisture change, we employed a *negative strict* variant of FR, retaining only pixels that exhibited negative change across all relevant bands. Specifically, changed pixels were required to satisfy $\Delta\mathrm{VV} < 0$, $\Delta\mathrm{VH} < 0$, and Δpolarization ratio < 0 for radar features, and $\Delta\mathrm{NDVI} < 0$, $\Delta\mathrm{SAVI} < 0$, and $\Delta\mathrm{NDMI} < 0$ for optical indices.

Crucially, the FR method provides an adaptive reference by anchoring each pixel to the statistical distribution of its local cluster rather than to a single fixed baseline value. This spatial adaptivity allows neighboring pixels that share similar spectral and structural properties to act as stabilizing references, thereby suppressing random noise and enhancing sensitivity to coherent, spatially structured change.

2.3.3 Clay Autoencoder

Clay is a pre-trained, self-supervised, foundation deep learning model developed specifically for Earth observation applications [90]. The model was created by Clay Foundation, a nonprofit organization, in collaboration with Development Seed, a geospatial software company [1].

Clay adopts a masked autoencoder (MAE) architecture, illustrated in Fig. 2. Clay's MAE architecture is developed on a Vision Transformer (ViT) paradigm, which allows for 2D images as input. Clay was trained on millions of Sentinel-2 and Sentinel-1 images alongside other remotely sensed datasets. During training, random patches of input imagery are masked, and the model learns to reconstruct the missing content, thereby enabling the model to capture both spatial and spectral context. As a result, Clay learns high-dimensional semantic representations of satellite imagery without requiring labeled data.

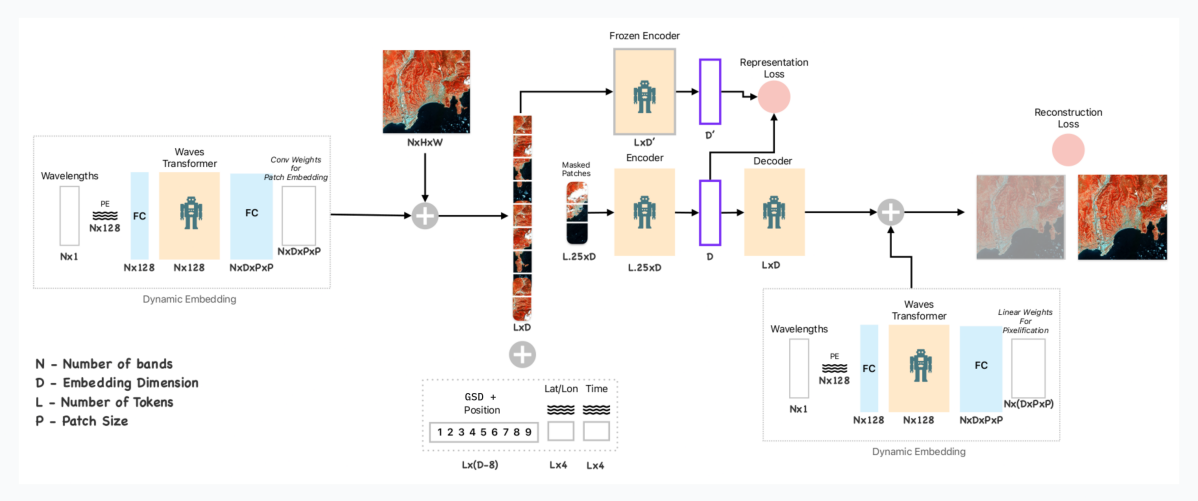

Figure 2: Clay model architecture, reproduced from Development Seed and Clay Foundation (2025). [32, 90].

This study adopted a *zero-shot* approach to identify drought-prone areas [83]. For each t_1 and t_2, both Sentinel-2 and Sentinel-1 composites were prepared and co-registered to ensure pixel-level alignment across modalities.

For Sentinel-2, each monthly composite $\mathbf{x}_t^{S2}$ was prepared, with each image comprising six channels: red, green, blue, NDVI, NDMI, and SAVI. Each composite covered an area of 2536×3396 pixels. Since Clay requires smaller inputs, each composite was tiled into 256×256 pixel segments. Tiles containing more than 80% valid data were retained, resulting in 75 clean tiles per composite per epoch.

For Sentinel-1, each composite $\mathbf{x}_t^{S1}$ contained the dual-polarized backscatter coefficients for VV and VH. To ensure spatial correspondence with Sentinel-2, each Sentinel-1 band was matched to the Sentinel-2 reference grid and resampled to 10 m resolution using bilinear interpolation. This alignment step ensured that each 256×256 Sentinel-1 tile corresponded exactly to its Sentinel-2 counterpart in both spatial extent and resolution.

When leveraging deep learning models, the data must be in the correct format [51]. To ensure compatibility with Clay's architecture, input data needed to be standardized and formatted

[1] Further details about Clay are available at https://clay-foundation.github.io

according to the model's specifications.

As Sentinel-2 composites were obtained from GEE, reflectance values were rescaled and clipped for red, green, and blue to ensure compatibility with Clay's training data. The red, green, and blue bands were then standardized using the mean and standard deviation values provided in Clay's metadata file. Although NDVI, NDMI, and SAVI were not part of the original Clay training configuration, they were included as additional input channels. These vegetation indices complemented the original spectral bands by introducing additional vegetation-sensitive information into the input feature space. This was intended to support the extraction of latent representations more responsive to vegetation stress and drought-related change. In the absence of metadata values for these indices, the per-channel mean and standard deviation from each composite were computed and standardized. Radar bands, VV and VH, were similarly standardized based on precomputed means and standard deviations from the Sentinel-1 dataset, as specified in the same metadata configuration. After standardization, all channels were clipped to the range of -3 to +3 to ensure optimal results [2]. Additional temporal and spatial metadata (e.g., timestamp, latitude, longitude, ground sampling distance, and wavelength) were also included in the input data structure to match Clay's expected input structure.

The model was executed on one tile at a time, allowing the entire process to be performed efficiently on CPU, without requiring a GPU. Within each 256 × 256 tile, Clay internally divides the image into 1024 non-overlapping 8 × 8 patches. Each patch is embedded into a 1 × 1024 semantic vector, resulting in one high-dimensional embedding per patch, plus a class token summarizing the tile. These embeddings served as the basis for change detection.

To detect drought-related change, the difference between pre- and post-drought embeddings was computed for each patch:

$$\Delta \mathbf{z}^{\mathrm{S2}} = \mathbf{z}_{t_2}^{\mathrm{S2}} - \mathbf{z}_{t_1}^{\mathrm{S2}} \tag{12}$$

$$\Delta \mathbf{z}^{\mathrm{S1}} = \mathbf{z}_{t_2}^{\mathrm{S1}} - \mathbf{z}_{t_1}^{\mathrm{S1}} \tag{13}$$

Given the high dimensionality of these vectors, principal component analysis (PCA) was applied to each set of differenced embeddings ($\Delta \mathbf{z}^{\mathrm{S2}}$ and $\Delta \mathbf{z}^{\mathrm{S1}}$) to reduce the complexity, extract meaningful latent patterns, and enable an effective investigation of the embedding vector [89]. The first and second principal components were analyzed to interpret potential drought signals and their spatial distributions for both Sentinel-1 and Sentinel-2 modalities.

It should be noted that, as the embeddings were constructed from an 8 × 8 patch within the 10 m input image, the resultant map represented change at an effective spatial resolution of ∼80 m.

2.4 Decision-Level Fusion of Optical and Radar Products

Once all change maps for each modality and method were generated, they were fused at decision level. For the baseline image differencing and FR methods, Sentinel-1 and Sentinel-2 binary change maps were fused using a discrete agreement scheme. Firstly, to enable decision-level fusion, Sentinel-1 generated drought maps were resampled to the 10 m Sentinel-2 reference grid using nearest-neighbor interpolation in order to preserve the categorical integrity [28]. Thereupon, final drought maps were generated with the following fusion rules where pixels were assigned a

value of 1 if change was detected by one sensor, and 2 if both sensors detected change. This approach emphasizes spatial agreement between optical and radar modalities while retaining sensitivity to uni-sensor changes.

For the Clay-based change maps, which represented continuous principal component outputs, correlation analyses were conducted between optical and radar component pairs to identify the most complementary drought-sensitive signals. PC_1 (optical) and PC_2 (radar) exhibited the strongest correlations with drought-sensitive indices (e.g., ΔNDVI, ΔNDMI, ΔVV, and ΔVH) and were therefore selected for fusion. The two components were standardized and fused through equal weight averaging. Equal weighting was adopted as a neutral fusion strategy, ensuring balanced contributions from both Sentinel-1 and Sentinel-2 without imposing an a priori preference for either modality in the absence of ground truth while also preserving the continuous nature of the Clay-derived change intensity fields. The resulting fused layer represents a single, latent multi-modal change map, where lower values indicate stronger negative change. A binary change map was subsequently derived using Otsu's thresholding [100], which provided a transparent and histogram-based threshold for converting the continuous fused layer into a binary change map without manual threshold selection.

2.5 Validation and Comparative Assessment

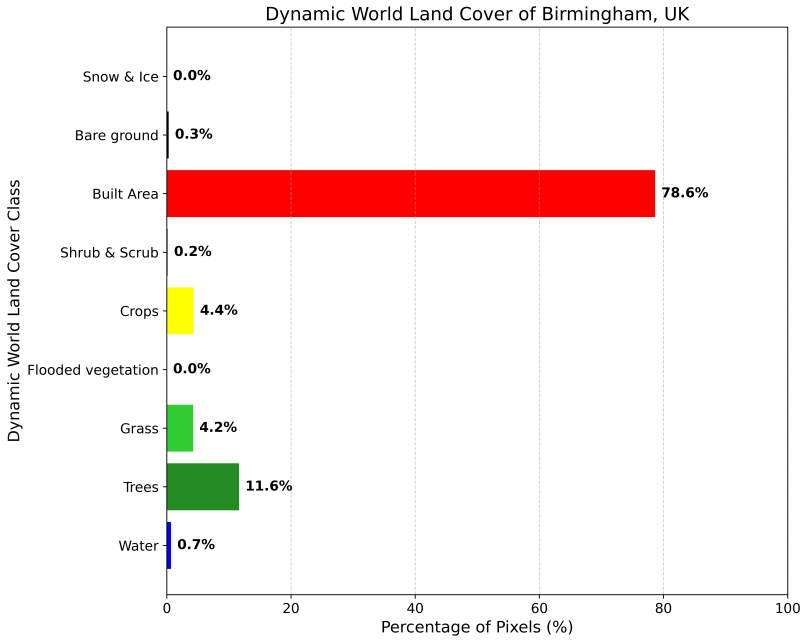

Figure 3: Distribution of land cover types within Birmingham, UK in July 2022.

As ground truthing is difficult to acquire [45], this study leveraged an indirect, multi-component interpretive assessment through thematic plausibility and spatial diagnostics rather than a formal accuracy assessment. Firstly, thematic plausibility was assessed through the Dynamic World land cover dataset, obtained from the GEE API. This product is created from Sentinel-2 at 10 m resolution, ensuring sensor and spatial compatibility with the 10 m change maps, although extra preprocessing steps were required to ensure alignment with the 80 m

Clay-derived outputs. Unlike typical land cover products that are derived annually, the Dynamic World product offers the advantage of near real-time updates [19]. This was beneficial for this study to facilitate comparisons between change maps and land cover data across the same temporal span, which was key to understanding which land cover experienced the most change.

Specifically, overlays and land cover composition summaries were used to determine whether mapped changes were concentrated in classes consistent with urban vegetation and whether differences among methods aligned with expected thematic patterns. This analysis was used as a contextual aid for interpretation only. Dynamic World was not treated as an independent reference dataset because it is derived from Sentinel-2 imagery and therefore does not constitute external ground truth. Moreover, Fig. 3 illustrates the percentage composition of land cover types across Birmingham in July 2022, providing contextual insight into the city's overall landscape makeup.

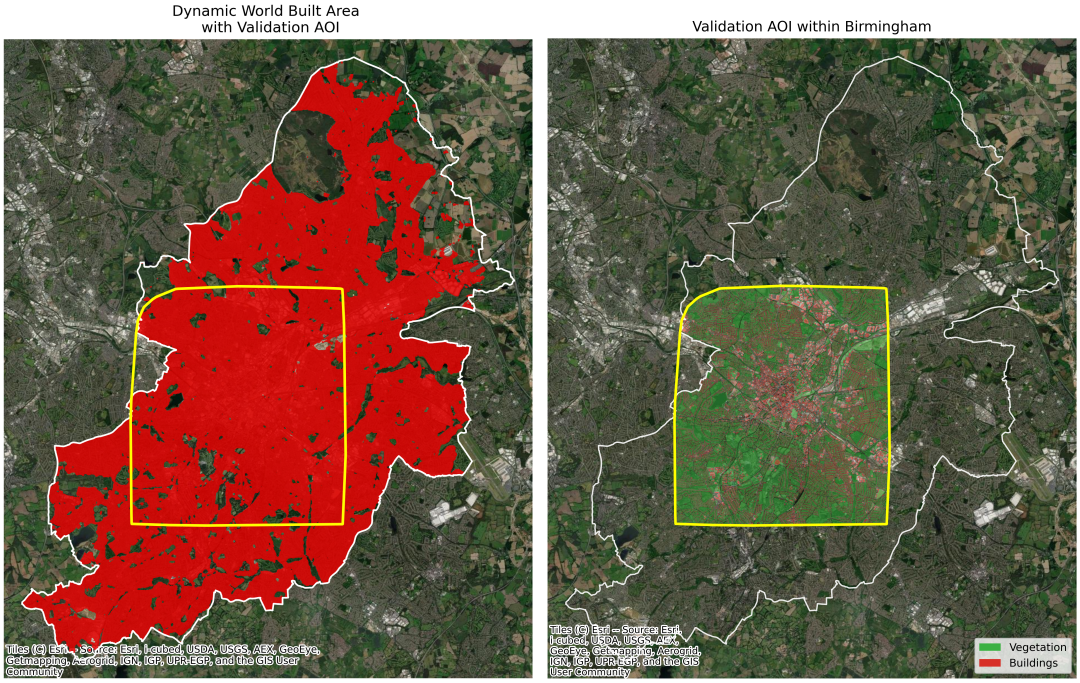

(a) (b)

Figure 4: Micro-validation study area to validate DW built area change. (**a**) DW built area land cover in Birmingham; (**b**) Micro-validation AOI with vegetation and building polygons.

Secondly, as the "built area" land cover dominated the study area, a micro-validation analysis was undertaken using high-fidelity ancillary datasets that are independent of the Sentinel imagery for Birmingham city center (Fig. 4). Building footprints were sourced from OpenStreetMap Buildings [72], high resolution greenspace polygons were obtained from Ordnance Survey MasterMap via Digimap [73], and tree point data were acquired from Birmingham City Council [9] and Birmingham Tree People [14]. These layers were reprojected to the common CRS, and the convex hull around all building footprints was used to define an AOI. Greenspace polygons were unioned with buffered tree locations (4 m) to represent vegetation. These layers were then rasterized on the 10 m baseline grid (vegetation supersedes buildings) to form a categorical reference for attributing change pixels. For Clay (80 m), this categorical layer was

upscaled by majority (mode) to align with the Clay grid.

Lastly, all generated change maps were compared in terms of spatial coherence and hotspot clustering to characterize the spatial organization of detected change. Global spatial autocorrelation was evaluated using Global Moran's I [26, 65] on each change map's native grid, preserving the original spatial resolution of the 10 m (baseline and FR) and 80 m (Clay principal component and binary) outputs. Hotspots were delineated through Local Moran's I [3] using a fixed spatial kernel (3×3 pixel neighborhood) and an 8-neighbor (queen) contiguity weighting scheme was primarily applied to preserve the spatial adjacency of pixels within the regular raster grid [4]. These metrics were used to compare the spatial coherence and clustering behavior of the different methods. Importantly, Moran's I measures spatial structure rather than classification correctness and was therefore used as a descriptive diagnostic, not as a measure of accuracy.

Altogether, these three components provide a structured basis for interpreting the outputs of the compared methods under data-scarce conditions. Rather than establishing absolute accuracy, the framework supports a cautious comparative evaluation of whether each method produces change patterns that are thematically plausible and spatially coherent.

3 Results

3.1 Spatial Context of Change Detected

Figure 5**a** shows the spatial distribution of the baseline image differencing and k-means thresholding, where only the top drought cluster was selected for fusion from both radar and optical products. The pixels categorized as '1', denoted in yellow, represent where only one modality detected drought, whilst the pixels shown in red categorized as '2' signify where both modalities delineated negative drought change. Furthermore, from **Table** 2, this method detected 5.92% change within Birmingham, where 5.6% was from one sensor detection and 0.32% where both sensors agreed on drought.

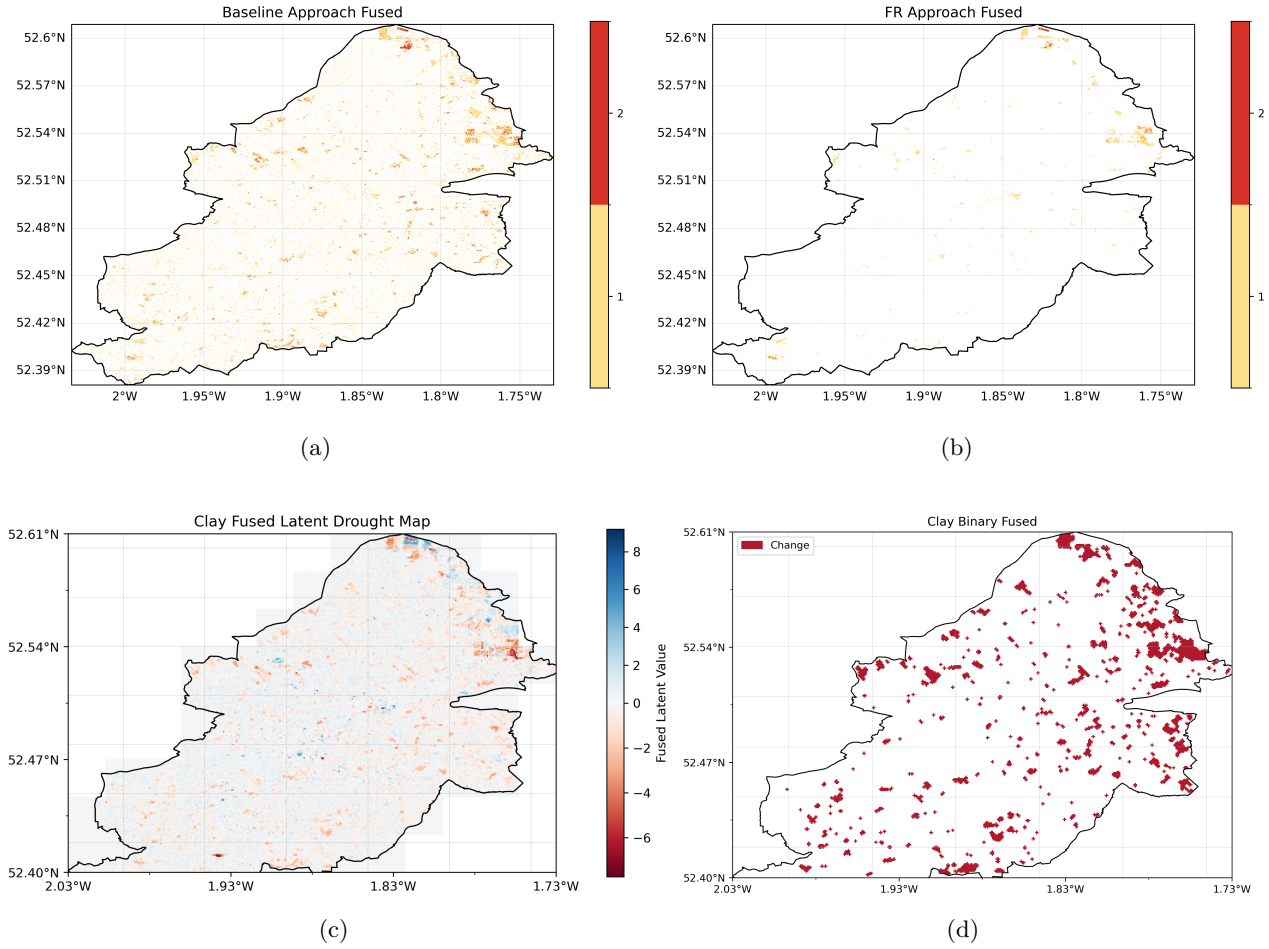

Figure 5: Comparative multi-modal fused change detection maps for Birmingham between July 2021 and July 2022. (**a**) Baseline differencing; (**b**) Floating References (FR); (**c**) Clay fused principal component; and (**d**) Clay binary. For panels (**a**) and (**b**), pixels labeled 1 represent single modality change detections, while pixels labeled 2 indicate agreement between both optical and radar detections. For panel (**c**), negative fused Clay principal component values are interpreted as drought-associated vegetation decline. Baseline and FR maps are shown at 10 m resolution, whereas Clay-derived maps reflect a coarser effective resolution of approximately 80 m.

On the other hand, the FR method ascertained a conservative 0.72% negative change within the AOI. **Figure** 5**b** presents a similar display of data to the baseline approach where pixels in which one modality detected change are characterized as '1' (yellow pixels), which accounted for 0.69% of the change. Whilst dual-modality agreement is shown through the red pixels, labeled as '2', that represented 0.03% change.

Table 2: Summary of changed vs. unchanged pixels for each change detection method

Method	**Changed (%)**	**Unchanged (%)**
Baseline	5.92	94.08
FR	0.72	99.28
Clay principal component	39.88	60.12
Clay binary	4.64	95.36

For both Clay principal component maps pre-fusion, the interpretation of positive and negative values was not immediately intuitive. Therefore, correlations with ΔNDVI and ΔNDMI maps and ΔVV and ΔVH maps were assessed to clarify drought directionality of optical and radar PCA products before fusion. $S2\_PC_1$, which explained 30.68% of the total variance, showed strong positive correlations with ΔNDVI (Pearson's $R = 0.834$, $p < 0.001$) and ΔNDMI ($R = 0.907$, $p < 0.001$), indicating that drought-associated change is represented by negative $S2\_PC_1$ values. Conversely, $S2\_PC_2$ accounted for 5.32% of the variance with weak negative correlations with both ΔNDVI ($R = -0.099$, $p < 0.001$) and ΔNDMI ($R = -0.105$, $p < 0.001$), suggesting that drought is expressed through positive $S2\_PC_2$ values. Due to $S2\_PC_1$'s stronger correlation to both ΔNDVI and ΔNDMI, it was chosen for the final fusion. The same process was conducted for $S1\_PC_1$ which explained 18.47% of the variance and showed a moderately strong correlation to ΔVV (Pearson's $R = 0.208$, $p < 0.001$) and ΔVH (Pearson's $R = 0.212$, $p < 0.001$). By contrast, $S1\_PC_2$ explained 5.32% of the variance, and showed a strong correlation to ΔVV (Pearson's $R = 0.602$, $p < 0.001$) and ΔVH (Pearson's $R = 0.590$, $p < 0.001$). Consequently, $S1\_PC_2$ was chosen for fusion due to its stronger correlation to ΔVV and ΔVH.

Figure 5**c** shows the Clay principal component map derived from the equal weight fusion of $S2\_PC_1$ and $S1\_PC_2$. In terms of extent, the Clay principal component map counted all negative values as negative drought-associated change, therefore showing the highest amount of change at 39.88%, as shown in **Table** 2. Subsequently, a binary map via Otsu's thresholding (**Figure** 5**d**) was generated from the principal component map, which exhibited change through red pixels that spanned across 4.64% of the study area.

Table 3: Global Moran's I for drought change maps on their native grids

Method	I	$\mathbf{E}[I]$	**z-score**	$p_{\mathbf{perm}}$
10 m grid				
Baseline	0.557	-0.00027	52.87	0.001
FR	0.494	-0.00027	46.91	0.001
80 m grid				
Clay fused (continuous)	0.468	-0.00001	258.19	0.001
Clay-binary	0.672	-0.00001	370.53	0.001

Table 3 summarizes the spatial coherence of each drought map in its native grid. The baseline and FR maps exhibited significant positive spatial autocorrelation (Moran's $I = 0.494$-0.557, $p = 0.001$), with the baseline showing slightly higher spatial coherence. On the Clay grid, the Clay binary map showed very strong clustering ($I = 0.672$, $p = 0.001$) compared to the Clay fused continuous field ($I = 0.468$, $p = 0.001$). The high z-scores associated with all methods ($\gg 0$) indicate that the observed I values deviate substantially from the expected value under spatial randomness ($\mathrm{E}[I] \approx 0$) [27], confirming that all detected drought patterns are highly structured rather than randomly distributed. Overall, the Clay binary and baseline maps exhibited the strongest spatial clustering of change on their respective grids.

Furthermore, **Table** 4 presents the resulting spatial clusters from Local Moran's I from the baseline approach. As the baseline map only contained change detections classified as either single sensor ('1') or dual sensor ('2') agreement, the High-High (HH) clusters repre-

Table 4: Local Moran's I cluster summary for the baseline map ($p < 0.05$).

Cluster type	Code	Count	Percent (%)
Not significant	0	10,958	78.60
HH (Hotspot)	1	1,037	7.44
LL (Coldspot)	2	926	6.64
LH (Outlier)	3	963	6.91
HL (Outlier)	4	58	0.42

sent areas where dual-modality change detections were spatially concentrated, indicating strong multimodal agreement and well-defined change hotspots. Low-Low (LL) clusters correspond to coherent regions of single sensor change detections, reflecting locally weaker or less consistent change detection. High-Low (HL) and Low-High (LH) outliers mark boundaries between single and dual sensor change detections or isolated detection anomalies. Local Moran's I identified significant spatial clustering across 21.4% of the AOI ($p < 0.05$). The HH clusters spanned 7.44% of the study area, signifying zones of strong Sentinel-1 and Sentinel-2 change agreement under drought conditions. In comparison, 6.64% of pixels formed LL clusters associated with single sensor detections, while 6.91% were LH outliers (single sensor pixels neighbouring dual sensor change zones). Only 0.42% of pixels were HL outliers, representing isolated dual sensor detections surrounded by single sensor change areas.

Table 5: Local Moran's I cluster summary for the FR map ($p < 0.05$).

Cluster type	Code	Count	Percent (%)
Not significant	0	4,637	73.39
HH (Hotspot)	1	287	4.54
LL (Coldspot)	2	1,092	17.28
LH (Outlier)	3	300	4.75
HL (Outlier)	4	2	0.03

Local Moran's I analysis for the FR map revealed significant spatial clustering across 26.6% of the study area ($p < 0.05$). As the map was similar to the baseline approach in its detection of single or dual sensor agreement, the change hotspots at 4.54% indicated relatively few but spatially coherent zones of dual sensor agreement. On the other hand, coldspots were more extensive at 17.28%, reflecting large areas of single sensor change detection. Outliers were predominantly of the LH type (4.75%), marking transitional boundaries between single and dual sensor detections, while HL outliers were negligible (0.03%) (**Table** 5). These results suggest that the FR approach produced more spatially significant clusters overall, with noticeably greater single sensor agreement compared with the baseline method.

To ensure consistent interpretation of hotspots and coldspots, the Clay principal component map values were inverted prior to Local Moran's I analysis so that higher values corresponded to stronger negative change. Following this adjustment, Local Moran's I identified significant spatial clustering across 21.6% of pixels ($p < 0.05$). As seen in **Table** 6, change hotspots covered 9.94% of the area, indicating coherent regions of elevated dual-modal change associated with drought, while coldspots covered 8.84%, representing locally coherent zones of lower change intensity. Spatial outliers were limited (LH 1.22%, HL 1.60%), consistent with sharp but sparse

Table 6: Local Moran's I cluster summary for the direction-corrected *Clay equal-weight fused* map ($p < 0.05$).

Cluster type	**Code**	**Count**	**Percent (%)**
Not significant	0	60,217	78.41
HH (Hotspot)	1	7,633	9.94
LL (Coldspot)	2	6,790	8.84
LH (Outlier)	3	935	1.22
HL (Outlier)	4	1,225	1.60

transition boundaries between affected and less affected areas. Overall, the fused principal component map delineated well-defined change clusters alongside compact, spatially coherent regions of vegetation resilience.

Table 7: Local Moran's I cluster summary for the *Clay binary* drought map ($p < 0.05$).

Cluster type	**Code**	**Count**	**Percent (%)**
Not significant	0	1,392	1.16
HH (Hotspot)	1	5,558	4.64
LL (Coldspot)	2	105,662	88.19
LH (Outlier)	3	7,196	6.01

Local Moran's I analysis for the Clay binary map revealed a highly coherent spatial structure, with significant clustering across 98.8% of pixels ($p < 0.05$). **Table** 7 presents that the map was dominated by LL clusters, which covered 88.19% of Birmingham and represented spatially consistent and stable areas. HH clusters occupied 4.64% of the area, delineating compact and robust change hotspots, while LH outliers comprised 6.01% of pixels, occurring primarily along boundaries between non-change and change regions. These results confirm that thresholding the fused principal component map using Otsu's method produced a stable binary change map with sharply defined hotspot boundaries and minimal spatial noise.

3.2 Land Cover Validation with Dynamic World

Table 8: Dynamic World land cover composition of detected change for each method. The changed-pixel composition reports the percentage of all detected changed pixels assigned to each land cover class, whereas the within-class change rate reports the percentage of pixels within each land cover class that were detected as changed.

Method	DW Class	Changed	Total	Composition (%)	Class Change (%)
Baseline	Water	2,776	29,954	0.5	9.3
	Trees	51,196	511,468	10.0	10.0
	Grass	72,813	185,810	14.3	39.2
	Flooded vegetation	3	46	0.0	6.5
	Crops	64,295	191,310	12.6	33.6
	Shrub & Scrub	1,524	6,828	0.3	22.3
	Built Area	313,040	3,454,868	61.4	9.1
	Bare ground	4,018	13,255	0.8	30.3
	Snow & Ice	0	8	0.0	0.0
Floating References	Water	732	29,954	1.2	2.4
	Trees	497	511,468	0.8	0.1
	Grass	4,306	185,810	6.9	2.3
	Flooded vegetation	0	46	0.0	0.0
	Crops	26,744	191,310	43.0	14.0
	Shrub & Scrub	110	6,828	0.2	1.6
	Built Area	25,976	3,454,868	41.8	0.8
	Bare ground	3,786	13,255	6.1	28.6
	Snow & Ice	0	8	0.0	0.0
Clay PC	Water	193	461	0.6	41.9
	Trees	3,888	7,784	12.7	49.9
	Grass	2,334	2,801	7.7	83.3
	Flooded vegetation	0	1	0.0	0.0
	Crops	1,717	2,919	5.6	58.8
	Shrub & Scrub	69	108	0.2	63.9
	Built Area	22,210	51,842	72.8	42.8
	Bare ground	87	152	0.3	57.2
	Snow & Ice	0	1	0.0	0.0
Clay Binary	Water	21	461	0.4	4.6
	Trees	597	7,784	10.8	7.7
	Grass	1,473	2,801	26.5	52.6
	Flooded vegetation	0	1	0.0	0.0
	Crops	1,164	2,919	21.0	39.9
	Shrub & Scrub	22	108	0.4	20.4
	Built Area	2,216	51,842	39.9	4.3
	Bare ground	57	152	1.0	37.5
	Snow & Ice	0	1	0.0	0.0

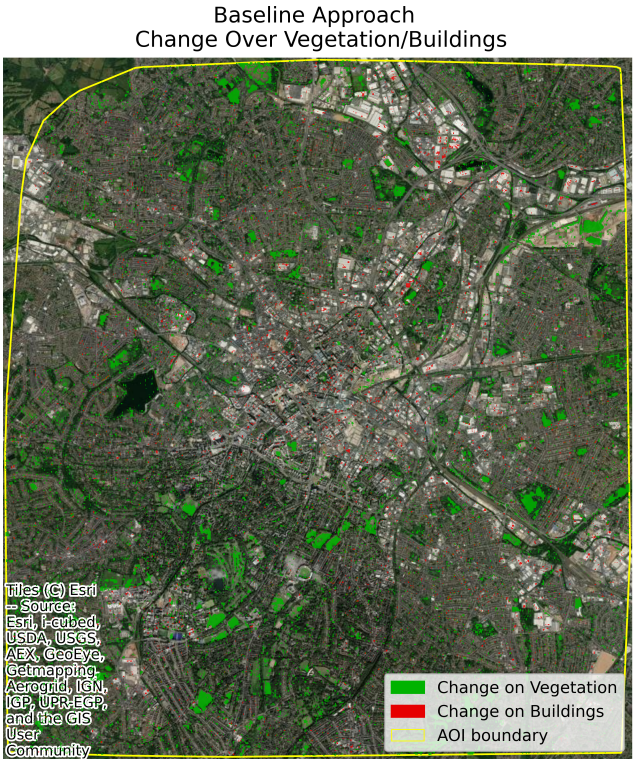

(a)

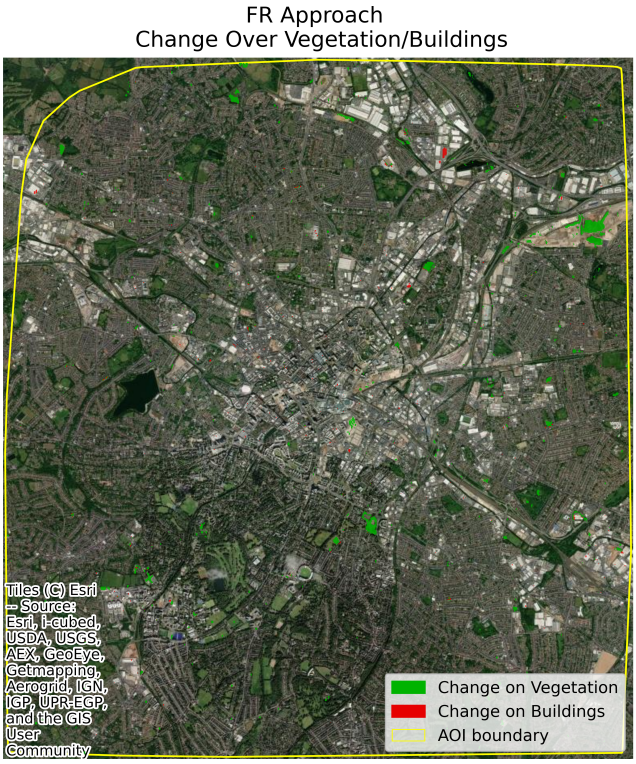

(b)

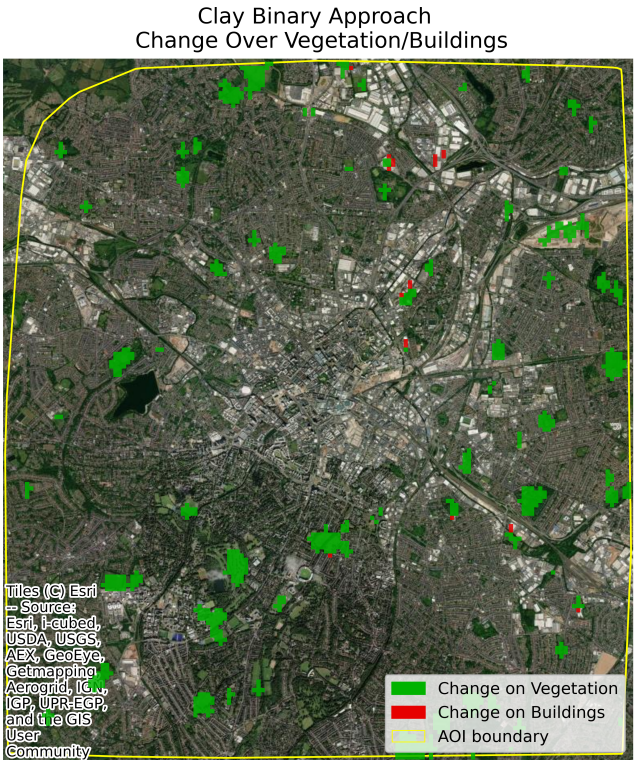

(c)

Figure 6: Change detected over vegetation and buildings for each method within the micro-validation study area. (**a**) Baseline differencing (10 m); (**b**) Floating References (FR; 10 m); and (**c**) Clay binary map, with vegetation and building reference layers resampled to match Clay's approximate 80 m effective resolution. The overlays are used to assess the spatial plausibility of detected vegetation change relative to local greenery and built structures.

Dynamic World land cover data were overlaid on each change detection map to provide a contextual interpretation of detected change across land cover classes during drought conditions. As shown in **Table** 8, two complementary summaries were considered: the composition of all detected changed pixels by land cover class and the within-class change rate, defined as the percentage of pixels within each Dynamic World class that were detected as changed. This distinction is important because dominant classes, particularly built area, may account for a large proportion of changed pixels simply due to their spatial extent, whereas the within-class change rate provides a normalized measure of relative change for each class.

For the baseline image differencing approach, built area represented the largest share of detected changed pixels (61.4%), followed by grass (14.3%), crops (12.6%), and trees (10.0%). However, when normalized by the total number of pixels in each class, the highest within-class change rates occurred in grass (39.2%), crops (33.6%), bare ground (30.3%), and shrub and scrub (22.3%), while built area exhibited a lower within-class change rate of 9.1%. This indicates that although built area contributed substantially to the overall composition of detected change, vegetative classes experienced proportionally greater change relative to their class extent.

The FR map showed a different pattern, with detected changed pixels primarily distributed across crops (43.0%) and built area (41.8%), followed by grass (6.9%) and bare ground (6.1%). The within-class change rates further indicated that bare ground (28.6%) and crops (14.0%) were the most proportionally affected classes, whereas grass (2.3%), trees (0.1%), and built area (0.8%) showed comparatively low within-class change. This suggests that the FR approach produced a more conservative change signal in vegetation, with a particularly strong response in cropland areas and limited proportional change in urban tree cover.

For the Clay-derived principal component map, built area comprised the largest share of detected changed pixels (72.8%), followed by trees (12.7%), grass (7.7%), and crops (5.6%). However, within-class change rates were high across several classes, including grass (83.3%), shrub and scrub (63.9%), crops (58.8%), bare ground (57.2%), trees (49.9%), and built area (42.8%). The Clay binary map showed a more vegetation-focused distribution of changed pixels, with grass (26.5%), crops (21.0%), and trees (10.8%) collectively accounting for a substantial proportion of detected change, while built area accounted for 39.9%. In the within-class analysis, grass (52.6%), crops (39.9%), bare ground (37.5%), and shrub and scrub (20.4%) showed the highest proportional change, whereas built area was substantially lower at 4.3%.

Notably, these results should be interpreted with consideration of the spatial scale mismatch between methods. The baseline and FR change maps were calculated using the 10 m Dynamic World grid, while the Clay PC and Clay binary maps were calculated using the 80 m Dynamic World grid to match the effective spatial resolution of the Clay-derived outputs. As a result, the Clay-based pixel counts are not directly comparable to those from the 10 m methods.

To further examine change within the DW "built area" class, the micro-validation dataset of vegetation and building polygons was intersected with the baseline, FR, and Clay binary maps (Fig. 6). As seen in **Table** 9, the FR (1 and 2 sensor) change map relative to the baseline, reduced the proportion of detections falling on building footprints from 13.26% (baseline) to 8.32%. This corresponded with a higher share of change mapped over vegetation at 63.66% for FR compared to the baseline at 60.16%. These results are consistent with FR's formulation,

which mitigates illumination and radiometric drift artefacts. Clay exhibited low building overlap (2.06%) and high vegetation proportion (86.58%), which is expected given both its semantic depth and the 80 m majority aggregation that suppresses rooftop artefacts. When restricting to two-sensor agreement only, the baseline approach produced substantially improved selectivity (92.41% vegetation; 1.17% buildings). In contrast, the FR two-sensor category was too small for robust interpretation (only 55 pixels) and is therefore not discussed further.

Table 9: Attribution of change pixels within DW built areas

Method	**Vegetation (%)**	**Buildings (%)**	**Other (%)**	**Npix**
Baseline (1 and 2 sensor)	60.16	13.26	26.58	133,825
Baseline (2 sensors)	92.41	1.17	6.41	3,915
FR (1 and 2 sensor)	63.66	8.32	28.02	11,433
FR (2 sensors)*	43.64	20.00	36.36	55
Clay Binary	86.58	2.06	11.35	872

*Small sample (N=55), percentages less stable and not used for interpretation.

3.3 Comparison across methods

Table 10 summarizes the advantages and drawbacks of each change detection approach evaluated in this study.

Firstly, the baseline image differencing method, coupled with k-means clustering, offered a straightforward, transparent, computationally efficient, and widely adopted strategy for pixel-wise change detection [23, 105]. Unlike traditional binary image differencing, this variant retained the strongest drought cluster which exhibited negative values across multiple indicators, such as NDVI, NDMI, and SAVI indices and VV and VH backscatter properties and their polarization ratio. This approach produced a spatially coherent map (Global Moran's $I = 0.557$, $p = 0.001$) and detected a relatively high proportion of spatially significant dual-sensor hotspots (7.44%), despite only 5.92% of the study area showing change overall (5.60% single-sensor and 0.32% dual-sensor). This indicates that although change was comparatively sparse, when it was detected, it often manifested in spatially coherent clusters. While simple and effective in highlighting areas of vegetation decline, this method flattened 2D spatial context into 1D vectors, thereby removing neighborhood relationships. Additionally, its reliance on direct pixel-based differences assumes that spectral or backscatter changes are meaningful indicators of ecological stress, which can introduce misclassifications arising from scene-specific illumination effects, drift, and phenological variation [56].

The FR method differed fundamentally from the baseline approach by assessing change relative to an adaptive reference derived jointly from both pre- and post-change epochs. This formulation mitigated biases arising from scene-specific illumination, phenological variation (i.e., natural seasonal or growth-stage differences in vegetation), and radiometric drift, thereby improving robustness to inter-annual variability and enhancing internal spatial coherence of clustered change compared to the baseline method. Consequently, the FR map produced the most conservative change estimates overall (0.72%), with the vast majority of detections arising from

Table 10: Comparison of change detection methodologies.

Method	Advantages	Limitations
Baseline Image Differencing + k-means	• Simple, transparent, and computationally efficient. • Captures spatially detailed vegetation change across several vegetated land cover classes. • Produces interpretable change maps with relatively high spatial autocorrelation (Global Moran's I) at 10 m, making it well suited for rapid assessments and fine-scale vegetation monitoring. • Increases the thematic plausibility of vegetation change detection when optical and radar agreement is enforced.	• Flattens spatial context into pixel-level vectors, losing neighborhood relationships. • Sensitive to scene-specific rooftop illumination and radiometric drift. • Increased misclassification of change within urban built-up areas, particularly with single-sensor detection.
Floating Reference (FR)	• Assesses change relative to an adaptive multi-date reference. • Mitigates bias from illumination, phenological variation, and inter-scene radiometric drift. • Produces compact and internally coherent change clusters, reflected in a relatively high proportion of spatially significant single-sensor hotspots. • Captures agricultural surface variability.	• Most conservative change detection across methods. • Computationally intensive and time consuming. • Limited detection in tree-dominated areas.
Clay Principal Component Map	• Utilizes pre-trained semantic embeddings without additional training. • Preserves spatial structure across 8×8 pixel patches. • Captures latent patterns linked to vegetation stress and canopy variation. • Shows sensitivity to semantically complex vegetation patterns, including mapped tree-dominated areas.	• Operates at coarser resolution ($\sim$80 m). • Abstract feature representations reduce interpretability. • Requires greater memory and preprocessing effort.
Clay Binary Drought Map (Otsu's Thresholded)	• Produces strong spatial coherence, as indicated by Global Moran's I. • Integrates spectral, textural, and semantic features into a single interpretable output. • Detects vegetation change patterns consistently across grass, crops, and trees. • Shows low sensitivity to building artefacts.	• Coarser spatial resolution ($\sim$80 m) limits local-scale interpretation. • Black-box nature of transformer-based embeddings reduces transparency. • More resource-intensive than pixel-based methods.

single-sensor divergence (0.69%). This outcome aligns with its formulation, which prioritizes internal consistency over magnitude, resulting in compact coherent clusters of single-sensor change detections (17.28%). However, this method was rendered the most computationally demanding of all methods due to its iterative centroid optimization.

The Clay-based principal component approach offered a deeply semantic, model-driven alternative. Clay effectively captured latent patterns relevant to vegetation drought-related stress while preserving spatial structure across 8×8 pixel patches through leveraging pre-trained

transformer embeddings, thus preserving spatial integrity. Moreover, given the limited availability of temporal observations at two epochs, the ability to extract meaningful representations without additional model training proved particularly advantageous. The resulting principal component map successfully delineated change even at a coarser spatial resolution (∼80 m). Furthermore, the binary change map derived via Otsu's thresholding from the aforementioned principal component map exhibited high spatial coherence ($I = 0.672$, $p = 0.001$) and captured drought-related change effectively. However, the increased spatial coherence of the resultant Clay maps should be interpreted partly as a scale effect, as coarser spatial resolution can smooth local variability and emphasize broader spatial structures rather than isolated pixel-level changes [98]. Additionally, this powerful framework introduced greater preprocessing complexity, demanded higher memory resources, and remained partially opaque due to the abstract nature of both the transformer-derived features and principal components, thus presenting itself in part as a methodological *black-box*.

To further contextualize how these patterns manifested across different surface types, Dynamic World land cover and micro-validation datasets were used to examine each method's sensitivity across surface types. The baseline approach identified substantial change across grass (14.3%), cropland (12.6%), and tree cover (10.0%), consistent with vegetation types most susceptible to drought [22]; however, it also exhibited elevated change within built-up areas (61.4%). The within-class change rates were highest for grass (39.2%), crops (33.6%), bare ground (30.3%), and shrub and scrub (22.3%), while built area showed a lower within-class change rate of 9.1%. This indicates that although built areas contributed substantially to the overall composition of detected change, vegetation-related classes experienced proportionally greater change relative to their mapped extent. Subsequent inspection confirmed that built area change was due to rooftop and impervious surface artefacts, although strict two-sensor agreement noticeably increased its thematic plausibility for fine-scale urban vegetation change detection.

By comparison, the FR approach produced a more conservative pattern of detected change. Croplands accounted for the largest share of changed pixels (43.0%), followed by built area (41.8%), grass (6.9%), and bare ground (6.1%). The within-class results further showed that bare ground (28.6%) and crops (14.0%) had the highest proportional change, whereas built area (0.8%), grass (2.3%), and trees (0.1%) remained comparatively low. The elevated bare ground response should be interpreted cautiously, as this class occupied a relatively small area and may include spectrally mixed or transitional surfaces such as sparsely vegetated land, exposed soil, dry grass, and construction sites. Overall, the FR method was less sensitive to widespread urban fabric artefacts and particularly responsive to agricultural surfaces.

The Clay PC map highlighted a relatively greater proportion of detected change within tree cover (12.7%), suggesting sensitivity to semantically complex vegetation patterns. Finally, the Clay binary map yielded a spatially coherent change map, with the largest proportions of detected change occurring in grass (26.5%), followed by crops (21.0%) and trees (10.8%), and the lowest proportion of detected change over built area (39.9%). In the within-class analysis, grass (52.6%), crops (39.9%), bare ground (37.5%), and shrub and scrub (20.4%) showed the highest proportional change, whereas built area was substantially lower at 4.3%. Micro-validation within

built area further indicated lower sensitivity to urban artefacts; however, the coarser aggregation can reduce fine-scale urban noise.

These findings reveal a clear methodological trade-off between spatial resolution, computational efficiency, and semantic richness. The baseline approach is well suited for high-resolution (10 m) mapping of vegetation change associated with drought conditions, providing interpretable and spatially detailed estimates at minimal computational cost. The Clay binary map offered strong semantic coherence as it integrated spectral, textural, and learned representational cues, which yielded plausible vegetation change across the study area. However, its coarser spatial resolution (∼80 m) plays a role in smoothing over artefacts and may not be well suited for fine-scale vegetation change analysis. The FR approach remains valuable as a stringent change detector, particularly for agricultural change. Overall, the combined insights from all three approaches yield a robust multi-scale understanding of vegetation change observed during the 2022 drought year, from detailed local vegetation patterns to broader landscape-level coherence.

4 Discussion

This study demonstrates the potential of unsupervised, multi-sensor change detection for mapping vegetation change associated with drought in a ground truth-scarce urban context. Rather than providing a definitive accuracy ranking, the analysis highlights how different unsupervised approaches capture complementary dimensions of change. Optical indices provided sensitivity to vegetation greenness and moisture status, while Sentinel-1 backscatter contributed information on canopy structure, surface roughness, and dielectric properties [16, 29, 58, 60, 64]. Together, these modalities enabled drought-associated vegetation change to be interpreted through both spectral and structural responses.

A central finding is that method choice strongly influences the spatial expression and thematic specificity of detected change. The baseline image differencing and k-means approach offered the clearest and most computationally efficient route to fine-scale change mapping. Its main strength lies in its transparency as changes can be directly traced to differences in vegetation indices and radar backscatter. However, this directness also makes the method more vulnerable to non-vegetation artefacts, particularly over rooftops, impervious surfaces, and other urban materials whose reflectance or backscatter may vary between acquisition periods. The reduction of these artefacts under stricter dual-sensor agreement suggests that multi-modal consistency is particularly important when applying simple pixel-based differencing in heterogeneous urban environments.

The FR approach provided a contrasting, more conservative strategy. By assessing change relative to an adaptive reference derived from both epochs, it reduced sensitivity to scene-specific differences and emphasized internally consistent change. This made it particularly suitable for surfaces with strong seasonal variability and dependence on soil moisture, such as croplands [55]. However, its conservatism also means that smaller or fragmented urban vegetation responses may be under detected, especially where vegetation is spatially mixed with built surfaces. This trade-off suggests that FR is valuable when false positives are a greater concern than omission, but may be less suited when the aim is to capture fine-scale urban greenery such as street trees or small greenspace patches.

The Clay-based approaches introduced a different set of strengths and limitations. The use of pre-trained latent representations allowed for change to be detected through broader spatial and semantic patterns rather than only through pixel-wise spectral differences. This produced spatially coherent outputs and reduced some fine-scale urban artefacts. However, this apparent improvement should not be interpreted solely as a methodological advantage. The effective ∼80 m spatial support of the Clay outputs contributed to greater coherence by smoothing local heterogeneity and reducing isolated pixel-level artefacts [98]. Consequently, Clay-derived maps are best interpreted as broader landscape-level indicators of drought-associated vegetation change, rather than as fine-scale maps of individual urban vegetation elements.

The land cover overlays further demonstrate the importance of interpreting detected change in relation to both class composition and within-class response. Vegetated classes, including grass, crops, and trees, were consistently associated with detected change, supporting the thematic plausibility of the mapped drought-year vegetation response. However, some classes require caution. Built-area detections may reflect genuine vegetation embedded within urban fabric, but may also arise from rooftop, shadow, or impervious-surface artefacts. Similarly, apparent change in bare ground should not be interpreted as vegetation drought response alone, as this class may include exposed soil, sparse vegetation, dry grass, construction sites, and disturbed or transitional land. Such detections may therefore reflect surface drying, land-use change, site management, or classification uncertainty in addition to drought-related vegetation stress.

These findings emphasize that the methods should be viewed as complementary rather than competing alternatives. The baseline approach is useful for transparent, high-resolution mapping where local detail is required, particularly when supported by optical and radar agreement. FR is most appropriate where conservative, internally consistent change detection is desired. The Clay binary map provides a semantically richer and spatially coherent perspective, but at the cost of reduced fine-scale interpretability. Together, the three approaches form a multi-resolution framework for assessing vegetation change associated with drought, spanning detailed local patterns through to broader landscape-level structure.

Despite their utility, several limitations must be acknowledged. First, the absence of ground truth data introduces uncertainty in the assessment of mapped change [5]; however, indirect validation using Dynamic World and vegetation overlays helped reinforce confidence. Dynamic World's class imbalance and Sentinel-2-derived nature constrain its ability to independently validate fine-scale urban vegetation such as street trees, pocket parks, and roadside greenery, although the added assessment of building footprint, greenspace, and tree point data within built area further helped contextualize urban vegetation change. Second, spatial mismatches between the 10 m inputs and ∼80 m Clay-derived embeddings introduced scale inconsistencies that influence spatial patterns, class summaries, and validation metrics. In particular, the greater spatial coherence and lower apparent sensitivity to urban artefacts observed in the Clay outputs may partly reflect the effects of smoothing due to coarser spatial resolution, rather than methodological differences alone [98]. Third, the bitemporal images capture observed interannual vegetation differences, which may reflect not only drought stress but other background influences such as phenological timing, site management, and local environmental conditions. This is

particularly relevant for mixed or transitional land-cover classes, such as bare ground, which may include exposed soil, sparse vegetation, construction sites, dry grass, or disturbed land. Detected change in these areas may therefore reflect surface drying, land-management activity, or classification uncertainty in addition to drought-related vegetation stress. Accordingly, this study interprets detected patterns as urban vegetation change associated with the 2022 drought summer, rather than attributing every mapped difference exclusively to drought.

Future research should leverage all change detection maps to generate a robust consensus agreement map, enabling drought-related change to be analyzed at the species level [21, 74, 77]. Additionally, alternative soft or fuzzy clustering frameworks, such as Gaussian mixture models (GMM) [24], Iterative Self-Organizing Data Analysis Technique Algorithm (ISODATA) [78], or Self-Organizing Map (SOM) [40], would be valuable to explore in future work as they may be well suited to detect drought-related vegetation change where boundaries between healthy and stressed vegetation can often be diffuse rather than discrete, particularly in heterogeneous urban environments [53, 86]. Furthermore, while the present analysis focused on Birmingham, U.K., the unsupervised nature of the framework supports its potential transferability to other urban contexts because it does not require labeled training data specific to the study area. Nevertheless, applying the framework across additional cities, climatic regions, urban forms, and drought events would be valuable for evaluating its robustness and for developing a wider understanding of vegetation resilience across differing climatic and urban contexts. In addition, the integration of L-band radar observations, particularly with the recently launched NASA-ISRO Synthetic Aperture Radar (NISAR), could enhance sensitivity to subsurface and structural moisture variations [6, 82]. Together, these advancements would further refine multi-sensor, multi-scale drought assessment frameworks for urban resilience monitoring.

Ultimately, this study demonstrates the potential of unsupervised methods for environmental, satellite-based change detection in data-scarce contexts. With no need for labeled training data or ground truth data, these methods span a spectrum of complexity from simple differencing to latent-space analysis and provide flexible, scalable tools for environmental monitoring.

5 Conclusions

As healthy urban vegetation plays a critical role in abating urban heat, it is vital to understand how drought affects these ecosystems. Therefore, this study demonstrated a multi-sensor, unsupervised framework for mapping urban vegetation change associated with the 2022 drought using optical and radar imagery under data-scarce conditions. By comparing three distinct change detection paradigms: baseline image differencing with k-means, floating references (FR), and representation-based learning via Clay, the analysis revealed that each method captures complementary aspects of vegetation change. The baseline approach provided a transparent and spatially detailed change map at 10 m resolution. Similarly at 10 m resolution, the FR technique offered conservative yet phenologically robust change detection, particularly suited to agricultural change. The Clay-derived binary map, leveraging pre-trained semantic embeddings, achieved spatial coherence and a semantically rich representation of vegetation change, though at $\sim$80 m resolution. These methods further highlight the value of integrating optical and radar modalities and unsupervised machine learning for comprehensive urban vegetation

change assessment. Future work should extend this study by generating a single robust agreement map to investigate species-level change, leveraging alternative clustering paradigms such as GMM, ISODATA, or SOM, applying the framework across diverse regions, and incorporating L-band radar. These extensions could support scalable monitoring of drought-associated vegetation change in complex urban landscapes, thereby informing more targeted recommendations for urban resilience planning.

Author Contributions

Conceptualization, Naya Desai and Emma Ferranti; Data curation, Naya Desai and Sarah Greenham; Formal analysis, Naya Desai; Funding acquisition, Emma Ferranti; Investigation, Naya Desai; Methodology, Naya Desai; Project administration, Emma Ferranti; Software, Naya Desai; Supervision, Emma Ferranti, Sarah Greenham, Joshua Vande Hey, Andrew Quinn and Stefano De Sabbata; Validation, Naya Desai; Visualization, Naya Desai, Sarah Greenham and Stefano De Sabbata; Writing – original draft, Naya Desai; Writing – review & editing, Naya Desai, Emma Ferranti, Sarah Greenham, Joshua Vande Hey and Stefano De Sabbata. All authors have read and agreed to the published version of the manuscript.

Funding

Ferranti & Greenham acknowledge funding from the Carmine (Project 101137851) funded by the European Union. UK participants in this project are co-funded by UK Research and Innovation (UKRI). J.D. Vande Hey acknowledges funding from the NIHR Health Protection Research Unit in Chemical Threats and Hazards.

Data Availability Statement

All data used in this study are open access data. Sentinel-2 and Sentinel-1 remote sensing satellite data are available from the Copernicus Open Access Hub (`https://scihub.copernicus.eu/` and Google Earth Engine (`https://earthengine.google.com/`) (accessed on 28 July 2025)). Dynamic World dataset can be found on Google Earth Engine (`https://developers.google.com/earth-engine/datasets/catalog/GOOGLE_DYNAMICWORLD_V1`), (accessed on 28 July 2025)).

Acknowledgments

The authors would like to acknowledge CARMINE, University of Birmingham, University of Leicester, and Clay for supporting this research.

Conflicts of Interest

The authors declare no conflicts of interest.

References

[1] Bashir Adamu, Sa'ad Ibrahim, Azad Rasul, Shittu J. Whanda, Philemon Headboy, Ibrahim Muhammed, and Isa Abubakar Maiha. Evaluating the accuracy of spectral indices from Sentinel-2 data for estimating forest biomass in urban areas of the tropical savanna. *Remote Sensing Applications: Society and Environment*, 22:100484, April 2021. ISSN 2352-9385. doi: 10.1016/j.rsase.2021.100484. URL `https://www.sciencedirect.com/science/article/pii/S2352938521000203`.

[2] Md Manjurul Ahsan, MA Parvez Mahmud, Pritom Kumar Saha, Kishor Datta Gupta, and Zahed Siddique. Effect of data scaling methods on machine learning algorithms and model performance. *Technologies*, 9(3):52, 2021.

[3] Luc Anselin. Local indicators of spatial association—lisa. *Geographical Analysis*, 27(2): 93–115, 1995. doi: https://doi.org/10.1111/j.1538-4632.1995.tb00338.x. URL `https://onlinelibrary.wiley.com/doi/abs/10.1111/j.1538-4632.1995.tb00338.x`.

[4] Luc Anselin, Ibnu Syabri, and Youngihn Kho. GeoDa : An Introduction to Spatial Data Analysis. *Geographical Analysis*, 38(1):5–22, 2006. ISSN 1538-4632. doi: 10.1111/j.0016-7363.2005.00671.x. URL `https://onlinelibrary.wiley.com/doi/abs/10.1111/j.0016-7363.2005.00671.x`. _eprint: https://onlinelibrary.wiley.com/doi/pdf/10.1111/j.0016-7363.2005.00671.x.

[5] P. M. Atkinson and G. M. Foody. Uncertainty in Remote Sensing and GIS: Fundamentals. In *Uncertainty in Remote Sensing and GIS*, pages 1–18. John Wiley & Sons, Ltd, 2002. ISBN 978-0-470-03526-9. doi: 10.1002/0470035269.ch1. URL `https://onlinelibrary.wiley.com/doi/abs/10.1002/0470035269.ch1`. Section: 1 _eprint: https://onlinelibrary.wiley.com/doi/pdf/10.1002/0470035269.ch1.

[6] Johannes Balling, Bart Slagter, Sietse van der Woude, Martin Herold, and Johannes Reiche. ALOS-2 PALSAR-2 ScanSAR and Sentinel-1 data for timely tropical forest disturbance mapping: A case study for Sumatra, Indonesia. *International Journal of Applied Earth Observation and Geoinformation*, 132:103994, August 2024. ISSN 1569-8432. doi: 10.1016/j.jag.2024.103994. URL `https://www.sciencedirect.com/science/article/pii/S1569843224003480`.

[7] Lucy J. Barker, Jamie Hannaford, Eugene Magee, Stephen Turner, Catherine Sefton, Simon Parry, Jonathan Evans, Magdalena Szczykulska, and Tracey Haxton. An appraisal of the severity of the 2022 drought and its impacts. *Weather*, 79(7):208–219, July 2024. ISSN 0043-1656, 1477-8696. doi: 10.1002/wea.4531. URL `https://rmets.onlinelibrary.wiley.com/doi/10.1002/wea.4531`.

[8] Alessia Benedetti, Matto Picchiani, and Fabio Del Frate. Sentinel-1 and sentinel-2 data fusion for urban change detection. In *IGARSS 2018-2018 IEEE international geoscience and remote sensing symposium*, pages 1962–1965. IEEE, 2018.

[9] Birmingham City Council. Birmingham city council homepage. https://www.birmingham.gov.uk/. Birmingham City Council, accessed 21 April 2026.

[10] Birmingham City Council. City of nature plan must be accepted by cabinet to meet birmingham's net-zero carbon target. https://www.birmingham.gov.uk/news/article/1057/city_of_nature_plan_must_be_accepted_by_cabinet_to_meet_birminghams_net-zero_carbon_target, January 2022. Published by Birmingham City Council, accessed 21 April 2026.

[11] Birmingham City Council. City retains tree city of the world status for fourth year running. https://www.birmingham.gov.uk/news/article/1305/city_retains_tree_city_of_the_world_status_for_fourth_year_running, March 2023. Published by Birmingham City Council, accessed 21 April 2026.

[12] Birmingham City Council. Birmingham becomes uk's first nature city. https://www.birmingham.gov.uk/news/article/1600/birmingham_becomes_uks_first_nature_city, July 2025. Published by Birmingham City Council, accessed 21 April 2026.

[13] Birmingham City Council. Projections | population and census. https://www.birmingham.gov.uk/info/20057/about_birmingham/1294/population_and_census/3, n.d. Birmingham City Council, accessed 21 April 2026.

[14] Birmingham Tree People. Birmingham tree people. https://birminghamtreepeople.org.uk/. Birmingham Tree People, accessed 21 April 2026.

[15] Birmingham Tree People, Birmingham City Council, Treeconomics, and Nature Based Solutions Institute. An urban forest master plan for birmingham 2021–2051: Executive report, 2021. Available at: https://birminghamtreepeople.org.uk/wp-content/uploads/2023/07/BUFMPExecReport-Final-Nov-2021-v1.pdf [Accessed 29 Oct. 2025].

[16] Else Linda Boogaard. Remote sensing assessment of the impact of the 2018 and 2019 droughts on the forests in The Netherlands, September 2021. URL https://essay.utwente.nl/89003/. Publisher: University of Twente.

[17] Marian Brestic and Marek Zivcak. PSII Fluorescence Techniques for Measurement of Drought and High Temperature Stress Signal in Crop Plants: Protocols and Applications. In Gyana Ranjan Rout and Anath Bandhu Das, editors, *Molecular Stress Physiology of Plants*, pages 87–131. Springer, India, 2013. ISBN 978-81-322-0807-5. doi: 10.1007/978-81-322-0807-5_4. URL https://doi.org/10.1007/978-81-322-0807-5_4.

[18] Guillaume Brigot, Elise Colin-Koeniguer, Aurélien Plyer, and Fabrice Janez. Adaptation and Evaluation of an Optical Flow Method Applied to Coregistration of Forest Remote Sensing Images. *IEEE Journal of Selected Topics in Applied Earth Observations and Remote Sensing*, 9(7):2923–2939, July 2016. ISSN 2151-1535. doi: 10.1109/JSTARS.2016.2578362. URL https://ieeexplore.ieee.org/document/7514244. Conference Name: IEEE Journal of Selected Topics in Applied Earth Observations and Remote Sensing.

[19] Christopher F. Brown, Steven P. Brumby, Brookie Guzder-Williams, Tanya Birch, Samantha Brooks Hyde, Joseph Mazzariello, Wanda Czerwinski, Valerie J. Pasquarella, Robert Haertel, Simon Ilyushchenko, Kurt Schwehr, Mikaela Weisse, Fred Stolle, Craig Hanson, Oliver Guinan, Rebecca Moore, and Alexander M. Tait. Dynamic World, Near real-time global 10 m land use land cover mapping. *Scientific Data*, 9(1):251, June 2022. ISSN 2052-4463. doi: 10.1038/s41597-022-01307-4. URL https://www.nature.com/articles/s41597-022-01307-4. Publisher: Nature Publishing Group.

[20] Dominik Brunner, Guido Lemoine, and Lorenzo Bruzzone. Earthquake damage assessment of buildings using vhr optical and sar imagery. *IEEE Transactions on Geoscience and Remote Sensing*, 48(5):2403–2420, 2010.

[21] F. Javier Cardama, Dora B. Heras, and Francisco Argüello. Consensus Techniques for Unsupervised Binary Change Detection Using Multi-Scale Segmentation Detectors for Land Cover Vegetation Images. *Remote Sensing*, 15(11):2889, January 2023. ISSN 2072-4292. doi: 10.3390/rs15112889. URL https://www.mdpi.com/2072-4292/15/11/2889. Publisher: Multidisciplinary Digital Publishing Institute.

[22] Jeremy Carter, S. M. Labib, and Ian Mell. Understanding and Assessing Climate Change Risk to Green Infrastructure: Experiences from Greater Manchester (UK). *Land*, 13(5): 697, May 2024. ISSN 2073-445X. doi: 10.3390/land13050697. URL https://www.mdpi.com/2073-445X/13/5/697. Number: 5 Publisher: Multidisciplinary Digital Publishing Institute.

[23] Turgay Celik. Unsupervised Change Detection in Satellite Images Using Principal Component Analysis and k-Means Clustering. *IEEE Geoscience and Remote Sensing Letters*, 6(4):772–776, October 2009. ISSN 1558-0571. doi: 10.1109/LGRS.2009.2025059. URL https://ieeexplore.ieee.org/abstract/document/5196726.

[24] Turgay Celik. Image change detection using Gaussian mixture model and genetic algorithm. *Journal of Visual Communication and Image Representation*, 21(8):965–974, November 2010. ISSN 1047-3203. doi: 10.1016/j.jvcir.2010.09.005. URL https://www.sciencedirect.com/science/article/pii/S1047320310001215.

[25] Guangliang Cheng, Yunmeng Huang, Xiangtai Li, Shuchang Lyu, Zhaoyang Xu, Hongbo Zhao, Qi Zhao, and Shiming Xiang. Change Detection Methods for Remote Sensing in the Last Decade: A Comprehensive Review. *Remote Sensing*, 16(13), June 2024. ISSN 2072-4292. doi: 10.3390/rs16132355. URL https://www.mdpi.com/2072-4292/16/13/2355.

[26] Andrew D. Cliff and John K. Ord. *Spatial Autocorrelation*. Pion Limited, London, 1973. ISBN 0850860369. A foundational text introducing statistical frameworks for spatial autocorrelation, extending Moran's I.

[27] Andrew D. Cliff and John K. Ord. *Spatial Processes: Models and Applications*. Pion Limited, London, 1981. ISBN 0850860814.

[28] J. W. Coulston, N. Zaccarelli, K. H. Riitters, F. H. Koch, and G. Zurlini. The spatial scan statistic: A new method for spatial aggregation of categorical raster maps, 2014. URL https://arxiv.org/abs/1408.0164.

[29] Ashim C. Das, Shihab A. Shahriar, Md A. Chowdhury, Md Lokman Hossain, Shahed Mahmud, Md Kamruzzaman Tusar, Romel Ahmed, and Mohammed Abdus Salam. Assessment of remote sensing-based indices for drought monitoring in the north-western region of Bangladesh. *Heliyon*, 9(2):e13016, February 2023. ISSN 2405-8440. doi: 10.1016/j.heliyon.2023.e13016. URL https://www.sciencedirect.com/science/article/pii/S2405844023002232.

[30] Vjosa Dervishi, Werner Poschenrieder, Thomas Rötzer, Astrid Moser-Reischl, and Hans Pretzsch. Effects of Climate and Drought on Stem Diameter Growth of Urban Tree Species. *Forests*, 13(5), April 2022. ISSN 1999-4907. doi: 10.3390/f13050641. URL https://www.mdpi.com/1999-4907/13/5/641.

[31] Adrià Descals, Karen Torres, Aleixandre Verger, and Josep Peñuelas. Evaluating Sentinel-2 for Monitoring Drought-Induced Crop Failure in Winter Cereals. *Remote Sensing*, 17(2):340, January 2025. ISSN 2072-4292. doi: 10.3390/rs17020340. URL https://www.mdpi.com/2072-4292/17/2/340. Number: 2 Publisher: Multidisciplinary Digital Publishing Institute.

[32] Development Seed. Clay: A foundation model for earth observation. https://developmentseed.org/projects/clay/, 2025. Accessed: 2025-07-20.

[33] European Space Agency. Sentinel-1. https://www.esa.int/Applications/Observing_the_Earth/Copernicus/Sentinel-1, . European Space Agency, accessed 21 April 2026.

[34] European Space Agency. Sentinel-2. https://www.esa.int/Applications/Observing_the_Earth/Copernicus/Sentinel-2, . European Space Agency, accessed 21 April 2026.

[35] Emma Ferranti, Anne Jaluzot, Sue James, and Kieron Doick. Trees as urban infrastructure. In *ICE Manual of Blue-Green Infrastructure*, ICE Manuals, pages 135–158. ICE Publishing, January 2023. ISBN 978-0-7277-6542-0. doi: 10.1680/icembgi.65420.135. URL https://www.icevirtuallibrary.com/doi/abs/10.1680/icembgi.65420.135.

[36] Eleonora Franceschi, Astrid Moser-Reischl, Martin Honold, Mohammad Asrafur Rahman, Hans Pretzsch, Stephan Pauleit, and Thomas Rötzer. Urban environment, drought events and climate change strongly affect the growth of common urban tree species in a temperate city. *Urban Forestry & Urban Greening*, 88:128083, October 2023. ISSN 1618-8667. doi: 10.1016/j.ufug.2023.128083. URL https://www.sciencedirect.com/science/article/pii/S1618866723002546.

[37] Bo-cai Gao. NDWI—A normalized difference water index for remote sensing of vegetation liquid water from space. *Remote Sensing of Environment*, 58(3):257–266, December 1996. ISSN 0034-4257. doi: 10.1016/S0034-4257(96)00067-3. URL https://www.sciencedirect.com/science/article/pii/S0034425796000673.

[38] Zijian Gao, Wen He, Yuefeng Yao, and Jinjun Huang. Revealing the Exacerbated Drought Stress Impacts on Regional Vegetation Ecosystems in Karst Areas with Vegetation Indices: A Case Study of Guilin, China. *Sustainability*, 17(3), February 2025. ISSN 2071-1050. doi: 10.3390/su17031308. URL https://www.mdpi.com/2071-1050/17/3/1308.

[39] Gohar Ghazaryan, Olena Dubovyk, Valerie Graw, Nataliia Kussul, and Jürgen Schellberg. Local-scale agricultural drought monitoring with satellite-based multi-sensor time-series. *GIScience & Remote Sensing*, 57(5):704–718, July 2020. ISSN 1548-1603. doi: 10.1080/15481603.2020.1778332. URL https://doi.org/10.1080/15481603.2020.1778332. Publisher: Taylor & Francis _eprint: https://doi.org/10.1080/15481603.2020.1778332.

[40] M. L. Gonçalves, M. L. A. Netto, J. A. F. Costa, and J. Zullo Júnior. An unsupervised method of classifying remotely sensed images using Kohonen self-organizing maps and agglomerative hierarchical clustering methods. *International Journal of Remote Sensing*, 29(11):3171–3207, June 2008. ISSN 0143-1161. doi: 10.1080/01431160701442146. URL https://doi.org/10.1080/01431160701442146. _eprint: https://doi.org/10.1080/01431160701442146.

[41] Sebastian Hafner, Andrea Nascetti, Hossein Azizpour, and Yifang Ban. Sentinel-1 and Sentinel-2 Data Fusion for Urban Change Detection Using a Dual Stream U-Net. *IEEE Geoscience and Remote Sensing Letters*, 19:1–5, 2022. ISSN 1558-0571. doi: 10.1109/LGRS.2021.3119856. URL https://ieeexplore.ieee.org/document/9570476.

[42] Sebastian Hafner, Yifang Ban, and Andrea Nascetti. Semi-Supervised Urban Change Detection Using Multi-Modal Sentinel-1 SAR and Sentinel-2 MSI Data. *Remote Sensing*, 15(21):5135, January 2023. ISSN 2072-4292. doi: 10.3390/rs15215135. URL https://www.mdpi.com/2072-4292/15/21/5135. Publisher: Multidisciplinary Digital Publishing Institute.

[43] Bijay Halder, Tiyasha Tiyasha, Shamsuddin Shahid, and Zaher Mundher Yaseen. Delineation of urban expansion and drought-prone areas using vegetation conditions and other geospatial indices. *Theoretical and Applied Climatology*, 149(3):1277–1295, August 2022. ISSN 1434-4483. doi: 10.1007/s00704-022-04108-2. URL https://doi.org/10.1007/s00704-022-04108-2.

[44] Txomin Hermosilla, Michael A. Wulder, Joanne C. White, and Nicholas C. Coops. Land cover classification in an era of big and open data: Optimizing localized implementation and training data selection to improve mapping outcomes. *Remote Sensing of Environment*, 268:112780, January 2022. ISSN 0034-4257. doi: 10.1016/j.rse.2021.112780. URL https://www.sciencedirect.com/science/article/pii/S0034425721005009.

[45] Hamed Heydari, , and Sayyed Bagher Fatemi Nasrabadi. Remote sensing change detection: a comparative study of spectral distances. *Geocarto International*, 38(1):2248059, December 2023. ISSN 1010-6049. doi: 10.1080/10106049.2023.2248059. URL https://doi.org/10.1080/10106049.2023.2248059. Publisher: Taylor & Francis _eprint: https://doi.org/10.1080/10106049.2023.2248059.

[46] A. R Huete. A soil-adjusted vegetation index (SAVI). *Remote Sensing of Environment*, 25(3):295–309, August 1988. ISSN 0034-4257. doi: 10.1016/0034-4257(88)90106-X. URL https://www.sciencedirect.com/science/article/pii/003442578890106X.

[47] Masroor Hussain, Dongmei Chen, Angela Cheng, Hui Wei, and David Stanley. Change detection from remotely sensed images: From pixel-based to object-based approaches. *ISPRS Journal of Photogrammetry and Remote Sensing*, 80:91–106, June 2013. ISSN 0924-2716. doi: 10.1016/j.isprsjprs.2013.03.006. URL https://www.sciencedirect.com/science/article/pii/S0924271613000804.

[48] Vera J. Hörmann, Ilhan Özgen Xian, Matthias Beyer, Malkin Gerchow, Mikael Gillefalk, Johannes Hoppenbrock, Michael W. Strohbach, Sebastian Preidl, and Mona Quambusch. Urban Tree Drought Stress: A Practitioner-Focused Review of Detection and Monitoring Methods. *Hydrological Processes*, 39(10):e70298, 2025. ISSN 1099-1085. doi: 10.1002/hyp.70298. URL https://onlinelibrary.wiley.com/doi/abs/10.1002/hyp.70298. _eprint: https://onlinelibrary.wiley.com/doi/pdf/10.1002/hyp.70298.

[49] A.K. Jain, R.P.W. Duin, and Jianchang Mao. Statistical pattern recognition: a review. *IEEE Transactions on Pattern Analysis and Machine Intelligence*, 22(1):4–37, January 2000. ISSN 1939-3539. doi: 10.1109/34.824819. URL https://ieeexplore.ieee.org/document/824819.

[50] Zainoolabadien Karim and Terence L. van Zyl. Deep/Transfer Learning with Feature Space Ensemble Networks (FeatSpaceEnsNets) and Average Ensemble Networks (AvgEnsNets) for Change Detection Using DInSAR Sentinel-1 and Optical Sentinel-2 Satellite Data Fusion. *Remote Sensing*, 13(21):4394, January 2021. ISSN 2072-4292. doi: 10.3390/rs13214394. URL https://www.mdpi.com/2072-4292/13/21/4394. Publisher: Multidisciplinary Digital Publishing Institute.

[51] Maksym Korobchynskyi and Vasiliy Nadraga. A systematic approach to data normalization and standardization in machine learning problems. In *Lecture Notes in Data Engineering, Computational Intelligence, and Decision-Making, Volume 2: 2024 International Scientific Conference" Intelligent Systems of Decision-Making and Problems of Computational Intelligence", Proceedings*, volume 244, page 206. Springer Nature, 2025.

[52] Katja Kowalski, Akpona Okujeni, and Patrick Hostert. A generalized framework for drought monitoring across Central European grassland gradients with Sentinel-2 time series. *Remote Sensing of Environment*, 286:113449, March 2023. ISSN 0034-4257. doi: 10.1016/j.rse.2022.113449. URL https://www.sciencedirect.com/science/article/pii/S0034425722005557.

[53] Leonie Leisenheimer, Thilo Wellmann, Clemens Jänicke, and Dagmar Haase. Monitoring drought impacts on street trees using remote sensing - Disentangling temporal and species-specific response patterns with Sentinel-2 imagery. *Ecological Informatics*, 82: 102659, September 2024. ISSN 1574-9541. doi: 10.1016/j.ecoinf.2024.102659. URL https://www.sciencedirect.com/science/article/pii/S1574954124002012.

[54] Zhongbin Li, Hankui K. Zhang, David P. Roy, Lin Yan, and Haiyan Huang. Sharpening the Sentinel-2 10 and 20 m Bands to Planetscope-0 3 m Resolution. *Remote Sensing*, 12(15):2406, January 2020. ISSN 2072-4292. doi: 10.3390/rs12152406. URL `https://www.mdpi.com/2072-4292/12/15/2406`. Publisher: Multidisciplinary Digital Publishing Institute.

[55] S. Liu, I. van Meerveld, Y. Zhao, Y. Wang, and J. W. Kirchner. Seasonal dynamics and spatial patterns of soil moisture in a loess catchment. *Hydrology and Earth System Sciences*, 28(1):205–216, 2024. doi: 10.5194/hess-28-205-2024. URL `https://hess.copernicus.org/articles/28/205/2024/`.

[56] D. Lu Corresponding author, Mausel , P., Brondízio , E., , and E. Moran. Change detection techniques. *International Journal of Remote Sensing*, 25(12):2365–2401, June 2004. ISSN 0143-1161. doi: 10.1080/0143116031000139863. URL `https://doi.org/10.1080/0143116031000139863`. Publisher: Taylor & Francis _eprint: https://doi.org/10.1080/0143116031000139863.

[57] Zhiyong Lv, Haitao Huang, Weiwei Sun, Tao Lei, Jón Atli Benediktsson, and Junhuai Li. Novel enhanced unet for change detection using multimodal remote sensing image. *IEEE Geoscience and Remote Sensing Letters*, 20:1–5, 2023.

[58] Dipankar Mandal, Vineet Kumar, Debanshu Ratha, Subhadip Dey, Avik Bhattacharya, Juan M. Lopez-Sanchez, Heather McNairn, and Yalamanchili S. Rao. Dual polarimetric radar vegetation index for crop growth monitoring using sentinel-1 SAR data. *Remote Sensing of Environment*, 247:111954, September 2020. ISSN 0034-4257. doi: 10.1016/j.rse.2020.111954. URL `https://www.sciencedirect.com/science/article/pii/S0034425720303242`.

[59] Valérie Masson-Delmotte, Panmao Zhai, Anna Pirani, Sarah L. Connors, Clotilde Péan, Sophie Berger, Nada Caud, Yang Chen, Leah Goldfarb, Melissa I. Gomis, Mengtian Huang, Katherine Leitzell, Elisabeth Lonnoy, J. B. Robin Matthews, Thomas K. Maycock, Tim Waterfield, Özge Yelekçi, Rong Yu, and Botao Zhou, editors. *Climate Change 2021: The Physical Science Basis. Contribution of Working Group I to the Sixth Assessment Report of the Intergovernmental Panel on Climate Change*. Cambridge University Press, Cambridge, United Kingdom and New York, NY, USA, 2021. doi: 10.1017/9781009157896.

[60] Heather McNairn and Jiali Shang. A review of multitemporal synthetic aperture radar (sar) for crop monitoring. *Multitemporal remote sensing: Methods and applications*, pages 317–340, 2016.

[61] Met Office. Midas open: Uk daily temperature data, v202507, 2025.

[62] Met Office. Midas open: Uk hourly rainfall data, v202507, 2025.

[63] David L. Miller, Erin B. Wetherley, Dar A. Roberts, Christina L. Tague, and Joseph P. McFadden. Vegetation cover change during a multi-year drought in Los Angeles. *Urban*

Climate, 43:101157, May 2022. ISSN 2212-0955. doi: 10.1016/j.uclim.2022.101157. URL https://www.sciencedirect.com/science/article/pii/S221209552200075X.

[64] David Montero, César Aybar, Miguel D. Mahecha, Francesco Martinuzzi, Maximilian Söchting, and Sebastian Wieneke. A standardized catalogue of spectral indices to advance the use of remote sensing in Earth system research. *Scientific Data*, 10:197, April 2023. ISSN 2052-4463. doi: 10.1038/s41597-023-02096-0. URL https://www.ncbi.nlm.nih.gov/pmc/articles/PMC10082855/.

[65] P. A. P. Moran. Notes on continuous stochastic phenomena. *Biometrika*, 37(1/2):17–23, 1950. ISSN 00063444, 14643510. URL http://www.jstor.org/stable/2332142.

[66] Gabriella Almeida Moço, Rogério Galante Negri, Luana Albertani Paumpuch, João Vitor Mariano Ribeiro, Adriano Bressane, and Cassiano Bortolozo. Unsupervised Change Detection Methods Applied to Landslide Mapping: Case Study in São Sebastião, Brazil. *Transactions in GIS*, 28(8):2626–2638, 2024. ISSN 1467-9671. doi: 10.1111/tgis.13256. URL https://onlinelibrary.wiley.com/doi/abs/10.1111/tgis.13256. _eprint: https://onlinelibrary.wiley.com/doi/pdf/10.1111/tgis.13256.

[67] Archana Mullapudi, Amol D. Vibhute, Shankar Mali, and Chandrashekhar H. Patil. A review of agricultural drought assessment with remote sensing data: methods, issues, challenges and opportunities. *Applied Geomatics*, 15(1):1–13, March 2023. ISSN 1866-928X. doi: 10.1007/s12518-022-00484-6. URL https://doi.org/10.1007/s12518-022-00484-6.

[68] Samreen Naeem, Aqib Ali, Sania Anam, and Muhammad Munawar Ahmed. An Unsupervised Machine Learning Algorithms: Comprehensive Review. *International Journal of Computing and Digital Systems*, 13(1):911–921, April 2023. ISSN 2210-142X. doi: 10.12785/ijcds/130172. URL https://journal.uob.edu.bh:443/handle/123456789/4777.

[69] Rogério G. Negri and Alejandro C. Frery. Unsupervised Change Detection Driven by Floating References: A Pattern Analysis Approach. *Pattern Analysis and Applications*, 24(3):933–949, August 2021. ISSN 1433-755X. doi: 10.1007/s10044-020-00954-w. URL https://doi.org/10.1007/s10044-020-00954-w.

[70] T. R. Oke. The energetic basis of the urban heat island. *Quarterly Journal of the Royal Meteorological Society*, 108(455):1–24, January 1982. ISSN 0035-9009, 1477-870X. doi: 10.1002/qj.49710845502. URL https://rmets.onlinelibrary.wiley.com/doi/10.1002/qj.49710845502.

[71] A-M Olteanu-Raimond, Linda See, Michael Schultz, G Foody, Michael Riffler, Tanja Gasber, Laurence Jolivet, Arnaud Le Bris, Yann Méneroux, Lanfa Liu, et al. Use of automated change detection and vgi sources for identifying and validating urban land use change. *Remote Sensing*, 12(7):1186, 2020.

[72] OpenStreetMap contributors. Openstreetmap [data set]. https://www.openstreetmap.org, 2026. Building footprint data extracted from OpenStreetMap, OpenStreetMap Foundation, available under the Open Database License (ODbL), accessed 21 April 2026.

[73] Ordnance Survey. OS MasterMap Greenspace Layer [geospatial data]. https://digimap.edina.ac.uk/, 2026. Using EDINA Digimap Ordnance Survey Service, accessed 21 April 2026.

[74] Spiros Papadopoulos, Georgia Koukiou, and Vassilis Anastassopoulos. Decision Fusion at Pixel Level of Multi-Band Data for Land Cover Classification—A Review. *Journal of Imaging*, 10(1):15, January 2024. ISSN 2313-433X. doi: 10.3390/jimaging10010015. URL https://pmc.ncbi.nlm.nih.gov/articles/PMC10817066/.

[75] Subir Paul, Laura Elena Cue la Rosa, Pedram Ghamisi, and Richard Gloaguen. Unsupervised annual change detection from optical-SAR fused satellite image time-series using 3D-CAE. *International Journal of Remote Sensing*, 44(5):1628–1642, March 2023. ISSN 0143-1161. doi: 10.1080/01431161.2023.2187724. URL https://doi.org/10.1080/01431161.2023.2187724. Publisher: Taylor & Francis _eprint: https://doi.org/10.1080/01431161.2023.2187724.

[76] Daifeng Peng, Xuelian Liu, Yongjun Zhang, Haiyan Guan, Yansheng Li, and Lorenzo Bruzzone. Deep learning change detection techniques for optical remote sensing imagery: Status, perspectives and challenges. *International Journal of Applied Earth Observation and Geoinformation*, 136:104282, February 2025. ISSN 1569-8432. doi: 10.1016/j.jag.2024.104282. URL https://www.sciencedirect.com/science/article/pii/S1569843224006381.

[77] A. Pérez-Hoyos, A. Udías, and F. Rembold. Integrating multiple land cover maps through a multi-criteria analysis to improve agricultural monitoring in Africa. *International Journal of Applied Earth Observation and Geoinformation*, 88:102064, June 2020. ISSN 1569-8432. doi: 10.1016/j.jag.2020.102064. URL https://www.sciencedirect.com/science/article/pii/S0303243419309146.

[78] Muhammad Tauhidur Rahman. Detection of Land Use/Land Cover Changes and Urban Sprawl in Al-Khobar, Saudi Arabia: An Analysis of Multi-Temporal Remote Sensing Data. *ISPRS International Journal of Geo-Information*, 5(2), February 2016. ISSN 2220-9964. doi: 10.3390/ijgi5020015. URL https://www.mdpi.com/2220-9964/5/2/15.

[79] Shoumik Rahman and Victor Mesev. Change Vector Analysis, Tasseled Cap, and NDVI-NDMI for Measuring Land Use/Cover Changes Caused by a Sudden Short-Term Severe Drought: 2011 Texas Event. *Remote Sensing*, 11(19):2217, January 2019. ISSN 2072-4292. doi: 10.3390/rs11192217. URL https://www.mdpi.com/2072-4292/11/19/2217. Number: 19 Publisher: Multidisciplinary Digital Publishing Institute.

[80] Percy Yvon Rakoto, Kaveh Deilami, Joe Hurley, Marco Amati, and Qian (Chayn) Sun. Revisiting the cooling effects of urban greening: Planning implications of vegetation types and spatial configuration. *Urban Forestry & Urban Greening*, 64:127266, September 2021. ISSN 1618-8667. doi: 10.1016/j.ufug.2021.127266. URL https://www.sciencedirect.com/science/article/pii/S1618866721002934.

[81] J. W. Rouse, R. H. Haas, J. A. Schell, and D. W. Deering. Monitoring vegetation systems in the Great Plains with ERTS. January 1974. URL https://ntrs.nasa.gov/citations/19740022614. NTRS Author Affiliations: Texas A&M Univ. NTRS Report/Patent Number: PAPER-A20 NTRS Document ID: 19740022614 NTRS Research Center: Legacy CDMS (CDMS).

[82] Thomas Roßberg and Michael Schmitt. Comparing the relationship between NDVI and SAR backscatter across different frequency bands in agricultural areas. *Remote Sensing of Environment*, 319:114612, March 2025. ISSN 0034-4257. doi: 10.1016/j.rse.2025.114612. URL https://www.sciencedirect.com/science/article/pii/S0034425725000161.

[83] Anastasiia Safonova, Gohar Ghazaryan, Stefan Stiller, Magdalena Main-Knorn, Claas Nendel, and Masahiro Ryo. Ten deep learning techniques to address small data problems with remote sensing. *International Journal of Applied Earth Observation and Geoinformation*, 125:103569, December 2023. ISSN 1569-8432. doi: 10.1016/j.jag.2023.103569. URL https://www.sciencedirect.com/science/article/pii/S156984322300393X.

[84] Sudipan Saha, Francesca Bovolo, and Lorenzo Bruzzone. Unsupervised Deep Change Vector Analysis for Multiple-Change Detection in VHR Images. *IEEE Transactions on Geoscience and Remote Sensing*, 57(6):3677–3693, June 2019. ISSN 1558-0644. doi: 10.1109/TGRS.2018.2886643. URL https://ieeexplore.ieee.org/abstract/document/8608001.

[85] Souad Saidi, Soufiane Idbraim, Younes Karmoude, Antoine Masse, and Manuel Arbelo. Deep-Learning for Change Detection Using Multi-Modal Fusion of Remote Sensing Images: A Review. *Remote Sensing*, 16(20):3852, January 2024. ISSN 2072-4292. doi: 10.3390/rs16203852. URL https://www.mdpi.com/2072-4292/16/20/3852. Publisher: Multidisciplinary Digital Publishing Institute.

[86] P. Schmitter, J. Steinrücken, C. Römer, A. Ballvora, J. Léon, U. Rascher, and L. Plümer. Unsupervised domain adaptation for early detection of drought stress in hyperspectral images. *ISPRS Journal of Photogrammetry and Remote Sensing*, 131:65–76, September 2017. ISSN 0924-2716. doi: 10.1016/j.isprsjprs.2017.07.003. URL https://www.sciencedirect.com/science/article/pii/S092427161730271X.

[87] Zongyao Sha, Yahya Ali, Yuwei Wang, Jiangping Chen, Xicheng Tan, and Ruren Li. Mapping the changes in urban greenness based on localized spatial association analysis under temporal context using modis data. *ISPRS International Journal of Geo-Information*, 7 (10):407, 2018.

[88] Maurice Shorachi, Vineet Kumar, and Susan C. Steele-Dunne. Sentinel-1 SAR Backscatter Response to Agricultural Drought in The Netherlands. *Remote Sensing*, 14(10):2435, January 2022. ISSN 2072-4292. doi: 10.3390/rs14102435. URL https://www.mdpi.com/2072-4292/14/10/2435. Publisher: Multidisciplinary Digital Publishing Institute.

[89] Daniel Smilkov, Nikhil Thorat, Charles Nicholson, Emily Reif, Fernanda B Viégas, and Martin Wattenberg. Embedding projector: Interactive visualization and interpretation of embeddings. *arXiv preprint arXiv:1611.05469*, 2016.

[90] Clay Foundation Team. Clay: A foundation model for earth observation. https://clay-foundation.github.io/model/index.html, 2024. Clay Foundation documentation, accessed 21 April 2026.

[91] Steve Turner. Why we are still in drought despite recent rain. https://www.ceh.ac.uk/news-and-media/blogs/why-we-are-still-drought-despite-recent-rain, October 2022. UK Centre for Ecology & Hydrology, accessed 21 April 2026.

[92] Marcel Urban, Christian Berger, Tami E. Mudau, Kai Heckel, John Truckenbrodt, Victor Onyango Odipo, Izak P. J. Smit, and Christiane Schmullius. Surface Moisture and Vegetation Cover Analysis for Drought Monitoring in the Southern Kruger National Park Using Sentinel-1, Sentinel-2, and Landsat-8. *Remote Sensing*, 10(9):1482, September 2018. ISSN 2072-4292. doi: 10.3390/rs10091482. URL https://www.mdpi.com/2072-4292/10/9/1482. Publisher: Multidisciplinary Digital Publishing Institute.

[93] Dani Varghese, Mirjana Radulović, Stefanija Stojković, and Vladimir Crnojević. Reviewing the Potential of Sentinel-2 in Assessing the Drought. *Remote Sensing*, 13 (17):3355, January 2021. ISSN 2072-4292. doi: 10.3390/rs13173355. URL https://www.mdpi.com/2072-4292/13/17/3355. Number: 17 Publisher: Multidisciplinary Digital Publishing Institute.

[94] Chris R. Vernon, Kendall Mongird, Kristian D. Nelson, and Jennie S. Rice. Harmonized geospatial data to support infrastructure siting feasibility planning for energy system transitions. *Scientific Data*, 10(1):786, November 2023. ISSN 2052-4463. doi: 10.1038/s41597-023-02694-y. URL https://www.nature.com/articles/s41597-023-02694-y. Publisher: Nature Publishing Group.

[95] Mariette Vreugdenhil, Wolfgang Wagner, Bernhard Bauer-Marschallinger, Isabella Pfeil, Irene Teubner, Christoph Rüdiger, and Peter Strauss. Sensitivity of sentinel-1 backscatter to vegetation dynamics: An austrian case study. *Remote Sensing*, 10(9):1396, 2018.

[96] Harry West, Nevil Quinn, and Michael Horswell. Remote sensing for drought monitoring & impact assessment: Progress, past challenges and future opportunities. *Remote Sensing of Environment*, 232:111291, October 2019. ISSN 0034-4257. doi: 10.1016/j.rse.2019.111291. URL https://www.sciencedirect.com/science/article/pii/S0034425719303104.

[97] Chantha Wongoutong. The impact of neglecting feature scaling in k-means clustering. *PLOS ONE*, 19(12):e0310839, December 2024. ISSN 1932-6203. doi: 10.1371/journal.pone.0310839. URL https://www.ncbi.nlm.nih.gov/pmc/articles/PMC11623793/.

[98] Curtis E. Woodcock and Alan H. Strahler. The factor of scale in remote sensing. *Remote Sensing of Environment*, 21(3):311–332, April 1987. ISSN 0034-4257. doi: 10.1016/

0034-4257(87)90015-0. URL https://www.sciencedirect.com/science/article/pii/0034425787900150.

[99] Aoran Xiao, Weihao Xuan, Junjue Wang, Jiaxing Huang, Dacheng Tao, Shijian Lu, and Naoto Yokoya. Foundation Models for Remote Sensing and Earth Observation: A Survey, June 2025. URL http://arxiv.org/abs/2410.16602. arXiv:2410.16602 [cs].

[100] Xiangyang Xu, Shengzhou Xu, Lianghai Jin, and Enmin Song. Characteristic analysis of Otsu threshold and its applications. *Pattern Recognition Letters*, 32(7):956–961, May 2011. ISSN 0167-8655. doi: 10.1016/j.patrec.2011.01.021. URL https://www.sciencedirect.com/science/article/pii/S0167865511000365.

[101] Osama Yousif and Yifang Ban. Fusion of SAR and optical data for unsupervised change detection: A case study in Beijing. In *2017 Joint Urban Remote Sensing Event (JURSE)*, pages 1–4, March 2017. doi: 10.1109/JURSE.2017.7924636. URL https://ieeexplore.ieee.org/abstract/document/7924636.

[102] Chunhui Yuan and Haitao Yang. Research on K-Value Selection Method of K-Means Clustering Algorithm. *J*, 2(2):226–235, June 2019. ISSN 2571-8800. doi: 10.3390/j2020016. URL https://www.mdpi.com/2571-8800/2/2/16.

[103] Zichen Yue, Shaobo Zhong, Wenhui Wang, Xin Mei, and Yunxin Huang. Phenology-Optimized Drought Index Reveals the Spatio-Temporal Patterns of Vegetation Health and Its Attribution on the Loess Plateau. *Remote Sensing*, 17(5):891, January 2025. ISSN 2072-4292. doi: 10.3390/rs17050891. URL https://www.mdpi.com/2072-4292/17/5/891. Number: 5 Publisher: Multidisciplinary Digital Publishing Institute.

[104] Jie Zhang, Qiaozhen Mu, and Jianxi Huang. Assessing the remotely sensed Drought Severity Index for agricultural drought monitoring and impact analysis in North China. *Ecological Indicators*, 63:296–309, April 2016. ISSN 1470-160X. doi: 10.1016/j.ecolind.2015.11.062. URL https://www.sciencedirect.com/science/article/pii/S1470160X1500713X.

[105] Yaoguo Zheng, Xiangrong Zhang, Biao Hou, and Ganchao Liu. Using combined difference image and k-means clustering for sar image change detection. *IEEE Geoscience and Remote Sensing Letters*, 11(3):691–695, 2013.